

Report of the IFR Barrel Replacement Review Committee

F. Forti, C. Hearty, Y. Karyotakis, J. Nash,
B. Ratcliff, J. Richman, N. Roe, B. Spaan, and J. Va'vra.

May 22, 2003

Abstract

In September 2002, *BABAR* management set up a working group to examine whether or not the physics program of *BABAR* justified a major upgrade of the barrel component of the IFR, which is used for muon and K_L^0 detection. If so, the group was to recommend a detector technology to be used for the replacement. The working group included proponents of each of the three technologies considered, consultants for various technical issues, and a review committee. This document is the report of the review committee to *BABAR* management. The executive summary includes the major findings and recommendations, and is followed by more a more detailed presentation of each of the technologies and the physics and engineering issues common to all three. The charge and activities of the working group are summarized in the appendices.

Contents

1	Executive Summary	4
1.1	Findings	4
1.1.1	Physics	4
1.1.2	Experimental Operations	4
1.1.3	Engineering and Mechanical	4
1.1.4	LST	5
1.1.5	RPC	6
1.1.6	Extruded Scintillator with Fiber Optic Readout by APDs	7
1.1.7	Decision Timeliness	8
1.2	Recommendations	8
2	Existing RPC System	9
3	Implications of <i>BABAR</i> Physics Goals for the IFR	12
3.1	Introduction and Roadmap	12
3.2	Solid angle coverage of IFR systems	12
3.3	Overview of Relevant Physics Processes	15
3.4	Examples of Relevant Physics Processes	18
3.4.1	$B \rightarrow K\ell^+\ell^-$, $B \rightarrow K^*\ell^+\ell^-$, and $B \rightarrow X_s\ell^+\ell^-$	18
3.4.2	Inclusive and exclusive $b \rightarrow u\ell^-\bar{\nu}$ decays	20
3.4.3	Lepton tagging for CP asymmetry measurements	27
3.5	Characteristics of the current IFR barrel	27
3.6	Simulation of Benchmark Designs	34
3.7	Conclusions	43
4	Common Engineering Issues	47
4.1	Description of the Flux Return and Limitations to Access	47
4.2	Engineering Issues	49
5	Resistive Plate Chamber technology	51
6	Limited Streamer Tube technology	53
6.1	LST Technology Overview	53
6.2	Robustness and Maturity	54
6.3	LST proposal for <i>BABAR</i>	55
7	Scintillator Technology	57

8	Recommendations	60
A	Organization of the IFR Barrel Replacement Committee	61
B	Charge to the IFR Barrel Replacement Review Committee	62

1 Executive Summary

This summary is divided into Findings and Recommendations. The organization and composition of the committee is presented in Appendix A, while the charge to the committee is in Appendix B.

1.1 Findings

1.1.1 Physics

1. There is a compelling physics case for requiring excellent muon detection efficiency with good pion rejection over the greatest possible portion of the solid angle in *BABAR*. The ability to reconstruct or reject K_L^0 efficiency should be maintained to the extent that it does not compromise muon identification.
2. The present *BABAR* Barrel IFR is marginal for muon identification in terms of the amount of absorber, a problem exacerbated by failure of the outermost RPC layer, which is inaccessible. It is desirable to add additional absorber to reduce the pion punch-through.
3. The proposed upgrade must be designed to last through the end of the decade at peak luminosity of $4 \times 10^{34} \text{ cm}^{-2}\text{s}^{-1}$.
4. The upgrade strategy must minimize the impact on total integrated luminosity by keeping the net incremental down time as small as possible.

1.1.2 Experimental Operations

1. The present Barrel RPC chamber efficiencies continue to deteriorate. Average chamber efficiencies extrapolate to below 50% well before 2005. Present muon identification performance is already inadequate for many applications.
2. A major shutdown of at least 4.5 months is planned in 2005 to replace radiation-damaged elements of the SVT, and to change machine elements in the interaction region for the high luminosity design. Shorter shutdowns are expected in 2003 and 2004.

1.1.3 Engineering and Mechanical

1. Chambers can be replaced in layers 1–18. Layer 19 cannot be reached.

2. Chambers are restricted to 22 mm thickness.
3. Additional absorber material can be added by replacing some of the detection planes with 2.2 cm brass plates. The number and radial distribution of brass plates is strictly limited by floor loading and/or earthquake stability requirements. Five additional layers of brass are required simply to compensate for the loss of layer 19.
4. Engineering plans to remove the barrel RPC chambers and to reinstall new detectors and brass inserts are well developed and reasonable. RPC chamber removal requires significant mechanical work. It is not plausible to remove the existing chambers without removing the magnet corner plates. This work requires the transfer of the EMC loads during the operation. Although this is not without potential risk, the risk is judged to be acceptable.
5. Chamber removal and re-installation will require approximately 6.5 months, plus substantial end effects including commissioning, if done in one down period. It may also be done over two down periods; e.g., 2.75 months in 2004 for the first two sextants, and 4.5 months in 2005 for the remaining 4 sextants, again not including end effects. It should be done in parallel with other required down times, and carefully optimized to minimize the total down time. A net impact on running time of two months or less appears to be possible. Early availability of the new detectors is a potential advantage in reducing the impact of the installation. New chambers should be installed as soon as practical, consistent with the smallest net impact on the integrated luminosity of *BABAR*.
6. The cost of the engineering portion of the barrel upgrade is a major portion of the total project cost and is independent of the technology chosen. The cost of this portion including EDIA, labor, and M&S was estimated in December 2002 to be approximately \$2.5M.

1.1.4 LST

1. LSTs are conceptually well understood and have been used in more than a dozen HEP experiments with adequate performance. More recently constructed experiments have had good operational experience. Good QA is essential.

2. The proposed system design is modular and robust with well-developed plans for QA.
3. Successful prototype tests have demonstrated robustness against the highest expected rates, and the integrated charge for the experimental lifetime. Aging tests need to be repeated with the final prototype.
4. A full-scale double layer pre-production prototype is needed to demonstrate good plateau stability and robustness in production devices. The demonstration will require 4 months.
5. The production path is clear. All chambers could be completed well before 2005. It is likely that many or even all chambers could be completed by end of summer 2004 if desirable. There is a single vendor (Pol. Hi. Tech) for the extrusions.
6. New front-end electronics and utilities are required, including a new gas system. As signals are similar to those from existing RPCs, the downstream portions of the dataflow and reconstruction can be utilized.
7. There has been good progress in building a team that brings significant new resources, both human and technical, to the IFR upgrade project.
8. The cost of the LST system is the middle of the three considered.

1.1.5 RPC

1. Despite substantial work during the last few years in *BABAR*, the physics and chemistry of the chambers remain poorly understood. No effective remediation procedure has been found to improve chamber efficiencies, which continue to decline.
2. Twenty-four endcap chambers installed in 2000 provide a large-scale prototype of many features of the new production. QA has improved since they were constructed. Some chambers suffer a loss of performance that is not understood, and new, unresolved problems continue to emerge such as the visible discharge patterns (and associated efficiency loss) around buttons in chamber 7.
3. If the proposed two-gap chambers had the average performance of the chambers installed in 2000, they would be adequate for the barrel.

4. A conceptual prototype of a two-gap RPC chamber has been demonstrated. Details of the chamber construction have not been finalized or verified in a pre-production prototype.
5. There is a single source for the chamber gaps (General Tecnica). The factory is fully committed for a substantial period to finish ATLAS, CMS, Alice, and Opera. *BABAR* could potentially squeeze in for barrel completion by 2005, but there is no chance for 2004.
6. This system uses existing electronics, and other utility systems, and infrastructure.
7. The RPCs are the lowest cost of the three options.

1.1.6 Extruded Scintillator with Fiber Optic Readout by APDs

1. Novel technology, providing excellent time resolution, makes this technology an attractive candidate for high rate experiments. Z resolution is provided from timing.
2. The use of extruded scintillator with wavelength shifting fiber readout has been successfully demonstrated by the MINOS experiment. WLS-fiber has been found to be suitable for other experiments, such as the readout of the ATLAS tile calorimeter.
3. The proposed readout of low light levels emerging from the WLS fiber in the magnetic field requires the use of high gain avalanche photo diode arrays that have not yet been demonstrated. MINOS uses photomultipliers.
4. A conceptual prototype using a cooled single pixel APD has been completed and is being actively studied. Light yields and timing resolution attainable need further study with this prototype.
5. A prototype using the multi-pixel APD will not be available for several (> 2) months.
6. The reliability of the multi-pixel APD system is unknown at this time, and requires about 4 months for prototype testing.
7. The system requires new electronics with timing. DIRC style electronics has been proposed to reduce overall costs and the technical effort required.
8. Scintillator is the highest cost of the three options.

1.1.7 Decision Timeliness

1. The physics case for the upgrade is clear.
2. Engineering concepts for installation are well understood.
3. A decision is required very soon in order to obtain funding approval and match funding cycles.
4. Little additional information bearing on the detector technology choice can be expected for several months.
5. The project must begin soon to meet the very tight schedule for complete installation no later than summer 2005.

1.2 Recommendations

1. In order to optimize the physics output for the next decade, *BABAR* should proceed with an upgrade to the Barrel IFR as soon as practical. This upgrade should include the following elements:
 - Removal of existing RPC Chambers.
 - Placement of 2.2 cm thick brass slabs into at least 5 slots (or 6 slots if possible, pending a final optimization of material placement and load restrictions).
 - Installation of detectors into the other 12–13 slots.
2. The detection system for the barrel upgrade should be double-gap LST chambers of 2.2 cm thickness. Pre-production double gap prototypes should be fabricated and thoroughly tested by May 1, 2003, and their performance reviewed immediately thereafter.
3. An ongoing internal review process is encouraged to provide timely review of technical, cost, schedule, and management issues associated with the upgrade.
4. The fabrication and installation of the Barrel upgrade should be optimized with respect to running schedules and other down time needs of PEP-II and *BABAR* so as to minimize the impact on the integrated luminosity.

2 Existing RPC System

As originally built, the muon and K_L^0 detection system for *BABAR* consisted of 19 layers of resistive plate chambers (RPCs) interleaved with the flux return iron in the barrel region and 18 layers in the forward and backward endcaps. Each detector gap contained a single layer of RPCs based on a bakelite and linseed oil design. A similar style of RPC had previously been successfully used by L3. However, there were some significant differences. The L3 design used a double layer of chambers in each detection gap, reducing the sensitivity to the performance of any individual chamber. The particle rates in L3 were also substantially lower than *BABAR*, consistent with expectations from cosmic rays, compared with 0.2–0.5 Hz/cm² in the *BABAR* barrel and 5–20 Hz/cm² in the endcap. With the anticipated PEP-II luminosity increases, these rate could increase by an order of magnitude by 2010. Under current operating conditions, each track deposits approximately 1 nC per RPC gap.

The *BABAR* and L3 chamber designs also differ in detail. The L3 electrode spacers have simple straight surfaces, which were changed into a “mushroom” shape for *BABAR* to improve HV performance. These then trapped uncured linseed oil, an effect that proved to be significant.

During initial *BABAR* operations, the temperature of the iron increased to as much as 34°C, in part due to the lack of cooling for the RPC electronics. The trapped linseed oil decreased in viscosity and leaked out of the spacer cavities into the active volume of the chamber. There, under the influence of electrostatic forces, it formed bridges between the anode and cathode planes. The resistance of these bridges is approximately 1/40th of the value that would be expected with fresh linseed oil due to high current through the material, and operation at elevated temperatures in $C_2H_2F_4$ gas. The resulting electrical shorts between the electrode planes reduced the efficiency in the region surrounding the short.

Although cooling was installed shortly thereafter, reducing the operating temperature to 24°C, efficiencies have continued to decline at a rate of approximately 1.2% per month (Fig. 1).

A fraction of the failures have been due to high voltage, gas system, or front-end electronics problems. Many of these have been fixed, and work is ongoing to fix the remainder. However, efforts to reverse or halt the underlying decline in efficiency have not been successful. The unsuccessful “remediation” tests have included reverse biasing, high current flow in an argon atmosphere with both normal and reversed HV polarity, and the flow of high-humidity gas.

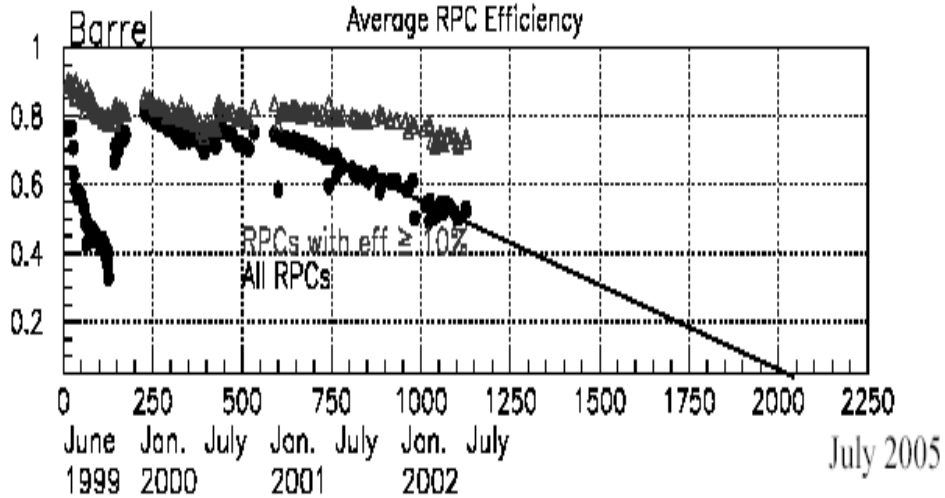


Figure 1: Average efficiency of the barrel RPC chambers as a function of date, in days since June 1999. (Full scale corresponds to July 2005). Bottom curve is the average of all chambers; top curve includes only those with efficiency greater than 10%.

To improve the particle identification efficiency of the forward endcap, and to establish the connection between the amount of linseed oil and the observed failures, 24 chambers were replaced in 12 layers of the forward endcap in November 2000. (The access to chambers is significantly easier in the endcaps than in the barrel). These were coated with approximately one-third the amount of linseed oil, and it was mixed with eptane instead of n-pentane. The surface felt much drier than the original. Otherwise, the replacements were constructed in the same fashion as the original set.

The efficiency of most of the new chambers remained stable, or showed only small drops in efficiency. However, layers 17 and 18 experienced high particle rates (1.2 Hz/cm^2 and 2.4 Hz/cm^2 respectively) and significant drops in efficiency, 13% and 45% over a 500 day period. It is assumed that this efficiency decrease is correlated with the total deposited charge. One other pair of chambers (layer 7) showed a drop in efficiency of 7–10%, although the particle rates were a low 0.1 Hz/cm^2 , similar to nearby chambers.

The layer 7 chambers were removed from *BABAR* in fall 2002 and opened, revealing many problems. Sparking was evident in several location, including along chamber edges, near linseed oil droplets located on the cathode,

and opposite a few whiskers. Approximately 5–10% of buttons showed signs of discharge with damage on the anode in the form of a “beam tree” image. Some beam tree images showed signs of anode surface deformation, compromising the anode-cathode gap quality, and indicating that a long-term discharge would deteriorate the chamber performance. There was also a sticky region around the beam tree buttons, indicating possible Freon-based chemistry during the discharge. The sticky regions seemed to have smaller surface resistivity. In addition, large bubbles had developed between the graphite and mylar on the exterior of the chamber at the locations of the large beam-tree spots.

Chambers from layer 14 were subsequently opened and showed similar features, although no significant drop in efficiency had been observed during the 500 days in which the chamber was operated.

All chambers in the forward endcap, including those installed in November 2000, were replaced in the summer and fall of 2002. These were produced with more stringent quality control than previous chambers and used a molded gas fitting that eliminated the need to drill holes in sealed chambers. The ability of the endcap to distinguish muons from pions was significantly improved by replacing 5 detector layers with 2.5 cm thick brass plates and adding 10 cm of steel to the back of the endcap. The two outermost detector planes were replaced by double layers of RPC chambers, significantly reducing the sensitivity of the detector to problems that are uncorrelated between the two chambers.

Although additional material was added beyond the final detector plane, backgrounds in some detector layers are too high (in early 2003) to permit the chambers to be operated. Work is under way to identify and shield the sources of these backgrounds. It may also be possible to reduce the amount of charge per track while retaining high detection efficiency by adding 1% SF₆ to the gas mixture. This gas mixture has been successfully tested on prototypes and will shortly be tested on one or more layers of the forward endcap.

3 Implications of *BABAR* Physics Goals for the IFR

3.1 Introduction and Roadmap

In the next few sections, we survey the role of the IFR in the current *BABAR* physics program and in the program that we foresee for the future. There are many *BABAR* physics analyses that use the IFR. Several are key measurements. Most IFR-related measurements involve processes with muons, such as semileptonic and leptonic decays of B , D , and D_s mesons; electroweak penguin decays such as $b \rightarrow s\ell^+\ell^-$; B decays to final states with J/ψ or $\psi(2S)$ mesons; and measurements that use muons for tagging, such as $B^0\bar{B}^0$ mixing and time-dependent CP asymmetry measurements. The IFR has also been successfully used for K_L^0 detection in the decay $B \rightarrow J/\psi K_L^0$.

We also consider the question of how the IFR hadron absorber can be modified to best match the needs of our future physics measurements. The issues that drive the design of the absorber configuration are largely independent of the detector technology.

We begin in Section 3.2 by examining the solid angle coverage of the different parts of the IFR. This provides a generic picture of how the loss of barrel RPC efficiency will affect our physics program. In Section 3.3, we list many of the measurements for which the IFR is used, and we give a rough guide to how much these measurements depend on the IFR. In Section 3.4 we discuss some of the important individual measurements in more detail. Because the new barrel IFR will not be fully installed until 2005, we focus on measurements that will be of long-term importance.

Section 3.5 discusses certain aspects of the current IFR barrel that relate to its performance in physics measurements. From this discussion, we conclude that it is desirable to install additional absorber material into the barrel. To explore the range of possibilities, we introduce three benchmark barrel designs, with different amounts and distributions of absorber. Section 3.6 compares the expected performance of these benchmark designs using GEANT Monte Carlo simulations.

Finally, in Section 3.7 we present our conclusions and respond to the specific, physics-related questions in the charge to the Committee.

The committee thanks Gianluca Cavoto, David Lange, and Ajit Mohapatra for their valuable contributions to this chapter.

3.2 Solid angle coverage of IFR systems

It is useful to evaluate impact of the loss of the IFR barrel in a generic way by computing the corresponding reduction in the total IFR acceptance in

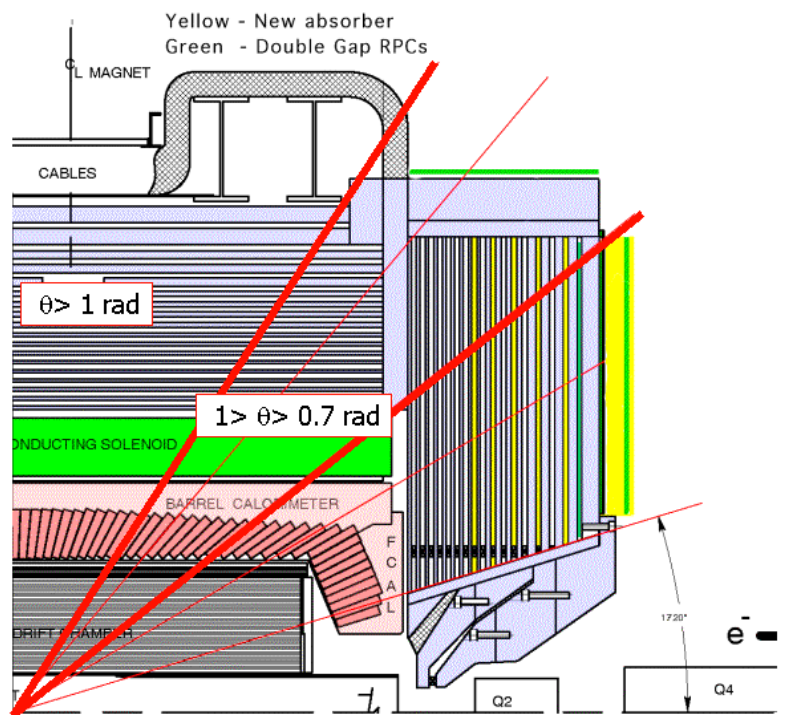


Figure 2: View of the barrel and forward endcap IFR.

the $\Upsilon(4S)$ rest frame (CM frame). Due to the unequal electron and positron beam energies, the CM frame is boosted with respect to the detector frame by $\beta\gamma = 0.55$ in the direction of the electron beam. This boost increases the importance of the forward region of the detector. Nevertheless, we will see that the barrel region covers a substantial part of the center-of-mass solid angle.

We define three angular regions, corresponding to the pure barrel region ($1 < \theta_{\text{lab}} < 2$ radians), the barrel/forward-endcap overlap region ($0.7 < \theta_{\text{lab}} < 1$ radian), and the pure forward endcap ($0.35 < \theta_{\text{lab}} < 0.7$ radian). Table 1 gives the fraction of CM solid angle covered by each region. We give three values, defined in the following way:

$$f(\cos \theta_{\text{CM}}) = \frac{1}{2} \int_{\text{IFR sub-region}} d \cos \theta_{\text{CM}}$$

$$f(\Omega_{\text{CM}}) = \frac{1}{4\pi} \int_{\text{IFR sub-region}} d \cos \theta_{\text{CM}} d\varphi$$

Table 1: Regions of the IFR and their coverage in the CM frame. We present three values. Column 3 lists the fraction of CM frame covered by different parts of the IFR, both ignoring gaps in azimuth $f(\cos\theta_{\text{CM}})$ and accounting for these gaps, $f(\Omega_{\text{CM}})$. Column 4 lists the fraction of the IFR acceptance provided by each part of the IFR. The backward IFR acceptance is not included, as explained in the text.

Region	Lab frame polar angles (radians)	Fract. of CM coverage $f(\cos\theta_{\text{CM}})$ [$f(\Omega_{\text{CM}})$]	Frac. of IFR coverage F_{IFR}
Pure barrel	$1 < \theta_{\text{lab}} < 2$	0.413 [0.380]	0.522
Bar./endcap overlap	$0.7 < \theta_{\text{lab}} < 1$	0.185 [0.170]	0.233
Pure endcap	$0.35 < \theta_{\text{lab}} < 0.7$	0.194 [0.178]	0.245
Sum	$0.35 < \theta_{\text{lab}} < 2.0$	0.792 [0.729]	1.0

$$F_{\text{IFR}} = \frac{\int_{\text{IFR sub-region}} d \cos \theta_{\text{CM}}}{\int_{\text{total IFR}} d \cos \theta_{\text{CM}}} \quad (1)$$

The “total IFR” includes the three regions listed above. It excludes the backward endcap, which we will discuss below. The acceptance calculations assume that the particles are relativistic, so that

$$\cos \theta_{\text{CM}} = \frac{\cos \theta_{\text{lab}} - \beta}{1 - \beta \cos \theta_{\text{lab}}}, \quad (2)$$

where $\beta \approx 0.48$.

These quantities are meant to give a simple picture of the geometrical acceptance of the IFR in the CM frame. The quantity $f(\cos\theta_{\text{CM}})$ simply gives the overall polar angle coverage of the different IFR regions, because the integral over $\cos\theta_{\text{CM}}$ is performed within the active detector region in φ . In contrast, the quantity $f(\Omega_{\text{CM}})$ reflects the loss of acceptance in the azimuthal cracks in the IFR. Due to the hexagonal structure of the detector, there are gaps in φ that amount to about 8% of the solid angle. We see that the overall geometric acceptance of the barrel plus forward endcap is about 73% of 4π .

To measure the *relative* importance of different IFR regions, we compute F_{IFR} , which is normalized to unity. From Table 1 we can see that, relative to the full barrel/forward-endcap system, the loss of the barrel would lead

to a reduction in our muon coverage of about 52% due to the loss of the pure barrel region; there would also be some degradation in performance over the additional 23% of our acceptance due to the barrel/forward-endcap overlap region. For most of the relevant muon momenta, the muons penetrate the iron completely, whereas pions stop sooner. As a consequence, the endcap chambers are more important than the barrel chambers for tracks in the overlap region. Thus, while loss of the barrel would degrade performance in the overlap region, the effect should not be too severe.

As mentioned earlier, we have ignored the backward endcap, which covers the polar angle region $2.0 < \theta < 2.7$ radians, or about 11% of $\cos \theta$ in the CM frame. However, the performance of these chambers is also declining, and there are no plans to replace them. Thus, by the time of the barrel replacement, the backward IFR endcap will be effectively absent. If the endcap were instead operational, then the barrel would represent about 46% of our muon acceptance rather than the 52% listed in the table.

To summarize, the loss of chamber efficiency in the IFR barrel represents about half of our muon acceptance. This loss will have a substantial effect on many physics analyses.

3.3 Overview of Relevant Physics Processes

In this section, we survey the measurements that depend on the IFR. This section is intended to give a broad overview of the relevant physics processes; more details on a small number of specific analyses will be given in Sec. 3.4.

According to present expectations, *BABAR* will have a data sample with integrated luminosity of roughly 239 fb^{-1} by the end of 2004 and about 363 fb^{-1} by the end of 2005. In the period from 2005–2009, it is projected that the total integrated luminosity is 1115 fb^{-1} . The difference, 752 fb^{-1} , is the data sample *BABAR* will acquire after the full installation of the new IFR barrel. Assuming that the experiment runs on resonance 85% of the time, then the $\Upsilon(4S)$ data sample will be 639 fb^{-1} , corresponding to about 700 M $B\bar{B}$ pairs. At the end of this period, the PEP-II peak instantaneous luminosity would be $23 \times 10^{33} \text{ cm}^{-2}\text{s}^{-1}$. If the IFR could be installed in 2004, then the total would be about 815 M $B\bar{B}$ pairs. With modifications to the interaction region, the data samples in the later years may be increased substantially, but we will not consider this possibility here.

What are the measurements in this time frame that will require the IFR? Table 2 lists the current or expected studies that benefit either from muon or K_L^0 detection capability. A large number of the current measurements will be continued in the future. In some cases, there is a clear and

Table 2: Measurements using the IFR

Process	Physics Goals	Role of muons	Role of K_L^0	Comments
$B \rightarrow \pi \ell^- \bar{\nu}, B \rightarrow \eta \ell^- \bar{\nu}, \dots$	BR, V_{ub} , dN/dq^2	***		stat, high p
$B \rightarrow \rho \ell^- \bar{\nu}, B \rightarrow \omega \ell^- \bar{\nu}, \dots$	BR, V_{ub} , dN/dq^2	***		stat, high p
$B \rightarrow X_u \ell^- \bar{\nu}$ (with B_{reco} sample)	BR, V_{ub}	***		stat, high p
$B \rightarrow X_u \ell^- \bar{\nu}$ (incl. endpoint)	BR, V_{ub}	***		high p
$B \rightarrow D \ell^- \bar{\nu}$	BR, V_{cb} , dN/dq^2	**		stat at high q^2
$B \rightarrow D^* \ell^- \bar{\nu}$	BR, V_{cb} , dN/dq^2	**		stat at high q^2
$B \rightarrow D_1 \ell^- \bar{\nu}, D_2^* \ell^- \bar{\nu}, D^{(*)} \pi \ell^- \bar{\nu}$	BR, V_{cb}	**		stat
$B \rightarrow X_c \ell^- \bar{\nu}$ (inclusive)	BR, V_{cb}	**		stat
$B \rightarrow X_c \ell^- \bar{\nu}$ (incl./ lepton tag)	BR, V_{cb}	**		stat
$B \rightarrow X_c \ell^- \bar{\nu}$ (mass moments)	BR, V_{cb}	**	* (?)	stat
$B \rightarrow D^{(*)} \tau^- \bar{\nu}$	BR, Higgs	**	* (?)	stat
$B \rightarrow K \ell^+ \ell^-$	BR, loops/new phys	****		stat
$B \rightarrow K^* \ell^+ \ell^-$	BR, loops/new phys	****		stat
$B \rightarrow X_s \ell^+ \ell^-$	BR, loops/new phys	***		stat
$B \rightarrow X_s \gamma$ (lepton tags)	BR, loops/new phys	**		stat
$B \rightarrow K \nu \bar{\nu}$	BR, loops/new phys		* (?)	stat
$B \rightarrow \mu^+ \mu^-$	BR, loops/new phys	***		stat
$B \rightarrow \tau^+ \tau^-$	BR, loops/new phys	***		stat
$B \rightarrow \tau \nu$	BR, new phys.	***	** (?)	stat
$B \rightarrow \mu \nu, B \rightarrow \mu \nu \gamma$	BR, new phys	****	** (?)	stat
$D_s \rightarrow \mu \nu$	BR, f_{D_s}	****		high p
$B \rightarrow J/\psi K_S^0$	CP , $\sin(2\beta)$	**		stat
$B \rightarrow J/\psi K_L^0$	CP , $\sin(2\beta)$	**	****	stat
$B \rightarrow J/\psi K^*$	CP , $\sin(2\beta)$	**		stat
$B \rightarrow J/\psi \eta, B \rightarrow J/\psi \bar{p} X, \dots$	rare decays	**		stat
$B \rightarrow J/\psi \pi^0$	CP	**		stat
$B^0 \bar{B}^0$ mixing	Δm_d	**		
$B^0 \bar{B}^0$ CP viol.	ϵ_B	**		stat
$\tau \rightarrow \mu \gamma$	New phys.	****		stat
J/ψ prod. w/init. state. rad.	leptonic widths	**		
$e^+ e^- \rightarrow \mu \tau$	New phys.	****		stat
$D \rightarrow K \ell \nu$	form factor	***		
$D \rightarrow K^* \ell \nu$	form factors	***		
$D \rightarrow \rho(\pi) \ell \nu$	form factors	***		stat

strong benefit from having a highly efficient IFR; in other cases the benefit is more incremental. In Table 2, we have grouped the processes into several categories:

1. $b \rightarrow u\ell^-\bar{\nu}$ decays,
2. $b \rightarrow c\ell^-\bar{\nu}$ decays,
3. electroweak penguin decays,
4. leptonic decays of B and D_s mesons
5. decays relevant to CP violation or mixing; decays involving charmonium.
6. a miscellaneous category that includes lepton-flavor violating processes and QCD studies using initial-state radiation.
7. semileptonic decays of charm mesons

We have made a rough evaluation of the importance of muon or K_L^0 detection in each case, based on a rating system, with one to four stars (*, **, ***, ****): * means that muon (or K_L^0) capability provides some benefit to the measurement, but the benefit is small; ** means that muon (or K_L^0) capability provides a significant benefit to the measurement; *** means that muon (or K_L^0) capability provides a large benefit to the measurement; **** means that muon (or K_L^0) capability is extremely important or essential to the measurement. The table also includes a list of comments in the right-hand column. The comment ‘stat’ indicates that the measurement is statistics limited. The comment ‘high p ’ indicates that the muons or K_L^0 have high momentum in the process listed. A hard muon momentum spectrum is an indication that the fake rate from misidentified pions can be further reduced by adding more absorber.

The loss of acceptance for muons will result not only in larger statistical uncertainties in the affected modes, but also in the loss of the valuable e vs. μ cross check. The sources of systematic errors associated with e and μ detection are quite different, mainly because different detection systems are used. In addition, electrons behave quite differently from muons in *BABAR* due to bremsstrahlung. There is a substantial amount of material associated with the Silicon Vertex Tracker (SVT) and the support tube, a cylinder that supports the SVT and beam-line components near the interaction point. As a consequence, bremsstrahlung from electrons passing through this material is important, and many analyses use so-called bremsstrahlung recovery

techniques that attempt to find the radiated photons. For example, in the $B \rightarrow Ke^+e^-$ analysis, bremsstrahlung recovery occurs in about 35% of events. While the efficiency for bremsstrahlung recovery can be effectively measured in data, a cross check on the branching fraction from muon data is valuable. The cross check provided by the muon channels can be important in high precision measurements such as the determination of $|V_{cb}|$ from $b \rightarrow c\ell^-\bar{\nu}$ transitions.

The importance of backgrounds from pions faking muons is highly mode dependent, and it can also depend greatly on the measurement technique. Thus, certain measurements may benefit from a lower $\pi \rightarrow \mu$ misidentification probability, but others will not. This issue will be discussed in more detail in the following section.

The overall picture that emerges from Table 2 is that a very broad range of measurements in the long-term *BABAR* physics program benefits significantly from muon identification. This is not surprising, given the importance of leptons in weak decays. Furthermore, many of these studies are highly important, including measurements needed to extract the magnitude of V_{ub} and the measurements of electroweak penguin processes.

Based on current ideas about the relevant physics topics, we believe that the benefits of K_L^0 identification and vetoing capabilities will be much more restricted. Thus, in our recommended configuration for the hadron absorber, we place greater emphasis on muon identification than was done in the past. However, our design still retains significant K_L^0 detection capability in the barrel IFR, since there may be either interesting physics processes involving K_L^0 that we have not yet considered, or analysis techniques available with a new detector technology.

3.4 Examples of Relevant Physics Processes

We now focus on some of the most important processes from Table 2, referring to existing *BABAR* analyses when possible. In the previous section, we noted that the size of the data sample for the period after the IFR barrel replacement is $700 - 800 \text{ fb}^{-1}$ or even more. For simplicity, in our examples below, we give yields (with and without the barrel IFR replacement) for 500 fb^{-1} . These yields can easily be scaled up to larger samples.

3.4.1 $B \rightarrow K\ell^+\ell^-$, $B \rightarrow K^*\ell^+\ell^-$, and $B \rightarrow X_s\ell^+\ell^-$

The electroweak penguin decays $B \rightarrow K\ell^+\ell^-$, $B \rightarrow K^*\ell^+\ell^-$, and $B \rightarrow X_s\ell^+\ell^-$ (inclusive) are an important part of the *BABAR* physics program.

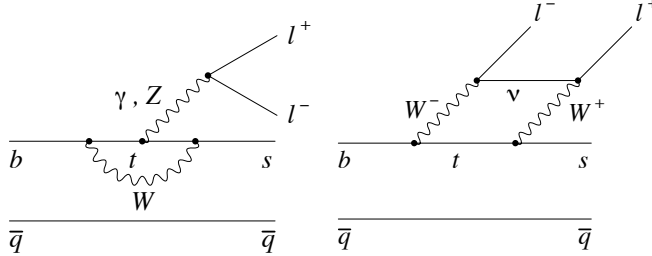


Figure 3: Standard Model processes for $B \rightarrow K^{(*)} \ell^+ \ell^-$: the electromagnetic (EM) and Z penguin diagrams (left) and the $W^+ W^-$ box diagram (right).

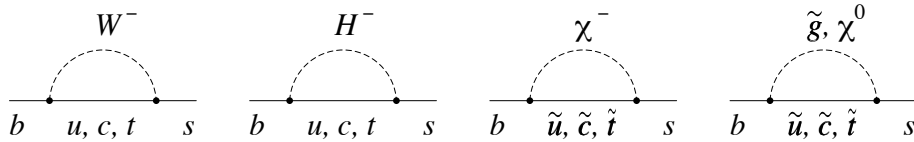


Figure 4: Contributions to the $b \rightarrow s$ transition from the SM model (far left diagram) and from new physics (remaining diagrams).

These processes involve highly suppressed loop diagrams in the Standard Model (Fig. 3) and are sensitive to certain types of contributions from new physics (Fig. 4). There is an extensive theoretical literature on these decays. In this discussion, we will focus only on experimental aspects directly related to the IFR.

BABAR and Belle have both observed $B \rightarrow K \ell^+ \ell^-$ (with large uncertainties), but neither experiment has so far observed $B \rightarrow K^* \ell^+ \ell^-$. In addition, Belle has observed the inclusive decay $B \rightarrow X_s \ell^+ \ell^-$. Because two leptons must be detected, these decays are quite sensitive to lepton ID performance. The signals so far are quite small, and these modes will be statistics limited for the lifetime of the experiment. In fact, future experiments with vastly larger samples, such as LHC-b, will continue to study the lepton forward-backward asymmetry in $B \rightarrow K^* \ell^+ \ell^-$, which is particularly sensitive to contributions from new physics.

Because the barrel IFR represents about half of the total IFR acceptance, loss of the barrel results in a dramatic reduction in efficiency—by a factor of four—for events with two uncorrelated leptons. A more precise (and somewhat higher) number for $B \rightarrow K^* \mu^+ \mu^-$ is given below.

The current *BABAR* analysis [1] for these electroweak penguin processes

observes a signal of $> 4\sigma$ in the $B \rightarrow K\ell^+\ell^-$ mode. There is a $\approx 3\sigma$ indication of a signal in the $B \rightarrow K^*\ell^+\ell^-$ mode. The signals in the combined electron and muons channels are shown in Fig. 5. Currently, however, most of the sensitivity comes from the electron channels, where the efficiency is typically *twice* that in the muon modes. (This is not the case for the Belle experiment, where the electron and muon mode efficiencies are comparable.) The efficiency for $B^+ \rightarrow K^+e^+e^-$ has been stable in time at about 19%, but Fig. 6 shows that the efficiency for $B^+ \rightarrow K^+\mu^+\mu^-$ has declined from 11.1% in year 2000, Block 1 to 9.1% in 2001, and finally to 5.9% in 2002. Similarly, for $B^+ \rightarrow K^{*0}\mu^+\mu^-$ the efficiency has dropped from 7.9% in Run 1 Block 1 to 6.5% in Run 2 (2001) to 3.8% in Run 2 (2002). (These values will be slightly different for the new version of this analysis, but the trends with time are the same.)

Similarly, the poor performance of the *BABAR* IFR has hampered the inclusive $B \rightarrow X_s\ell^+\ell^-$ measurement. While Belle has observed a significant signal in this crucial mode, the low efficiency in the muon channel has reduced the sensitivity of the *BABAR* analysis.

If the IFR barrel ceased to function (but the endcap was functional), we would lose roughly 2/3 of the $B \rightarrow K^*\mu^+\mu^-$ events [2]. Thus, in a $500 \text{ fb}^{-1} \mathcal{Y}(4S)$ data sample, the combined yield in $B^0 \rightarrow K^+\mu^+\mu^-$ and $B^0 \rightarrow K_S^0\mu^+\mu^-$ would fall from about 70 events to 23 events. The combined yield in $B \rightarrow K^*\mu^+\mu^-$ modes would fall from about 56 events to 19 events. These numbers assume efficiencies based on the tight muon selector and year 2000 block 1 run conditions. In the same sample, we expect 120 $B \rightarrow Ke^+e^-$ events and 110 $B \rightarrow K^*e^+e^-$. Note that the branching fraction for $B \rightarrow K^*e^+e^-$ is expected to be higher than $B \rightarrow K^*\mu^+\mu^-$ due to a larger contribution from the pole at $q^2 = 0$.

Figure 7 shows the quantities S/\sqrt{B} and $S/\sqrt{S+B}$ for individual $B \rightarrow K\mu^+\mu^-$ and $B \rightarrow K^*\mu^+\mu^-$ modes for scenarios with and without the IFR barrel upgrade. The quantity S/\sqrt{B} is the discovery significance: it measures the size of the signal relative to the size of fluctuations of the background. The quantity $S/\sqrt{S+B}$ is a measure of the expected precision on the central value. In the time frame we are considering, this latter quantity is more relevant. It is clear that the IFR barrel upgrade will significantly improve our sensitivity for these modes.

3.4.2 Inclusive and exclusive $b \rightarrow u\ell^-\bar{\nu}$ decays

The first part of Table 2 lists the most important semileptonic $b \rightarrow u$ transitions that can be used for extracting $|V_{ub}|$. The comprehensive study of these

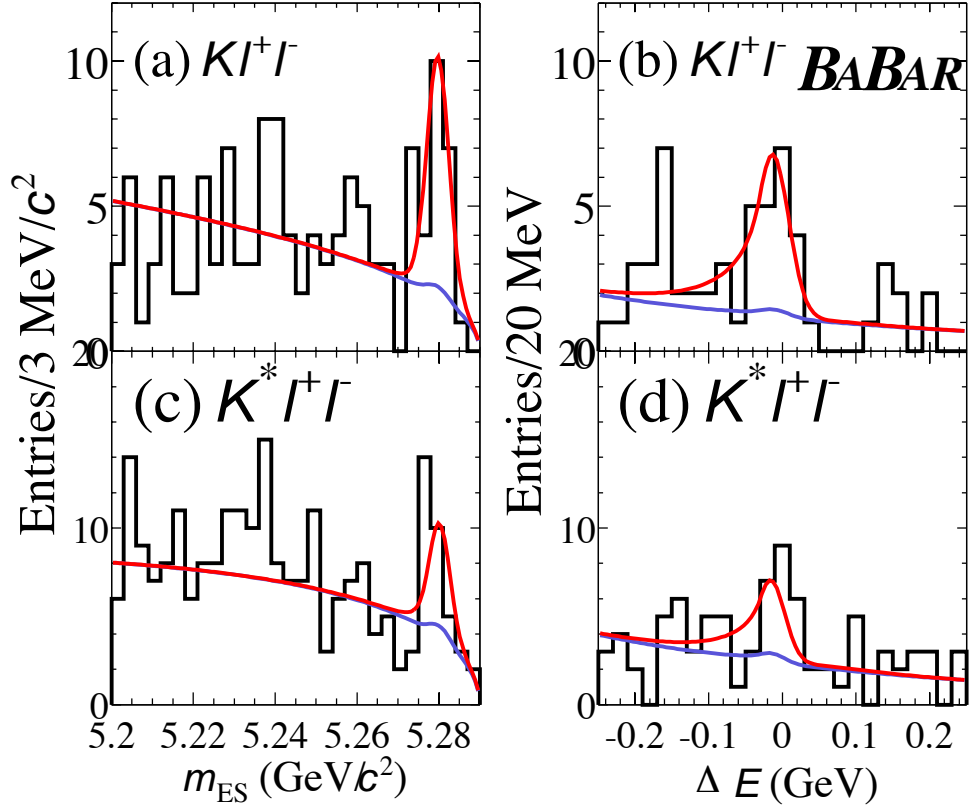


Figure 5: *BABAR* $B \rightarrow K l^+ l^+$ signals in (a) m_{ES} and (b) ΔE distributions for 84.4 M $B\bar{B}$ pairs. Each distribution is summed over electron and muon channels, as well as over B^+ and B^0 decays. A possible hint of a signal for $B \rightarrow K^* l^+ l^+$ is seen in (c) and (d), but the significance is below 4σ . The fitted background shape is shown in blue, while the total (signal plus background) is shown in red. The study of both exclusive and inclusive $b \rightarrow s l^+ l^-$ decay is a long-term goal of *BABAR*.

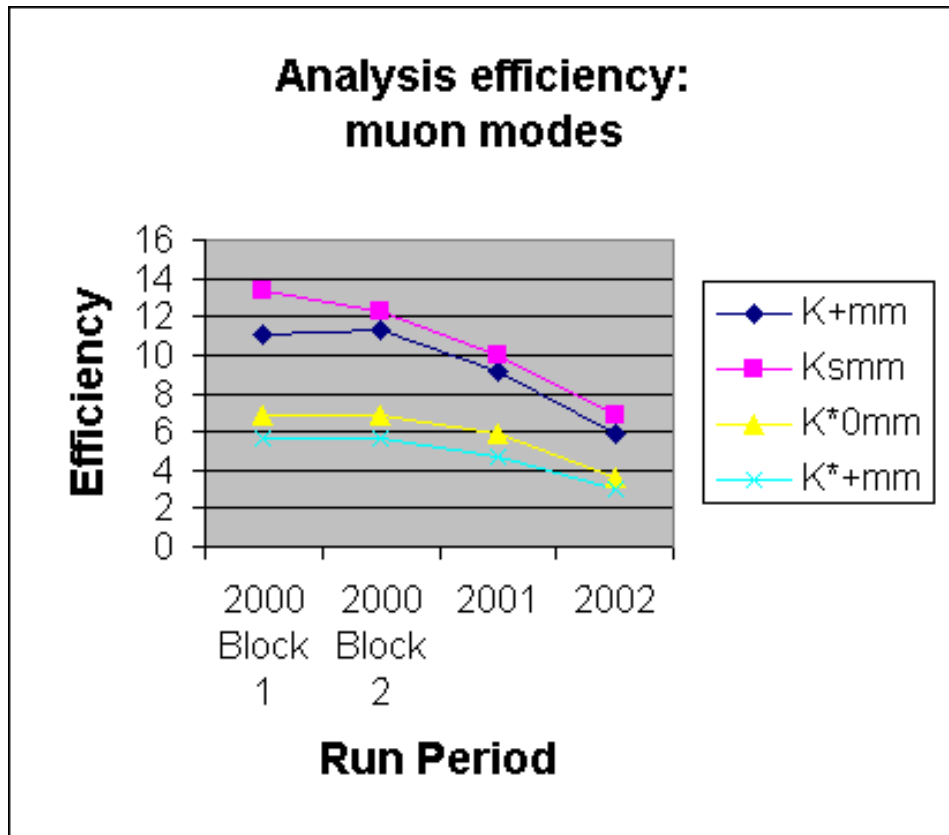


Figure 6: Detection efficiency vs. run period for $B \rightarrow K^{(*)}\mu^+\mu^-$ modes. In the corresponding electron modes, the efficiencies are higher and are stable with time.

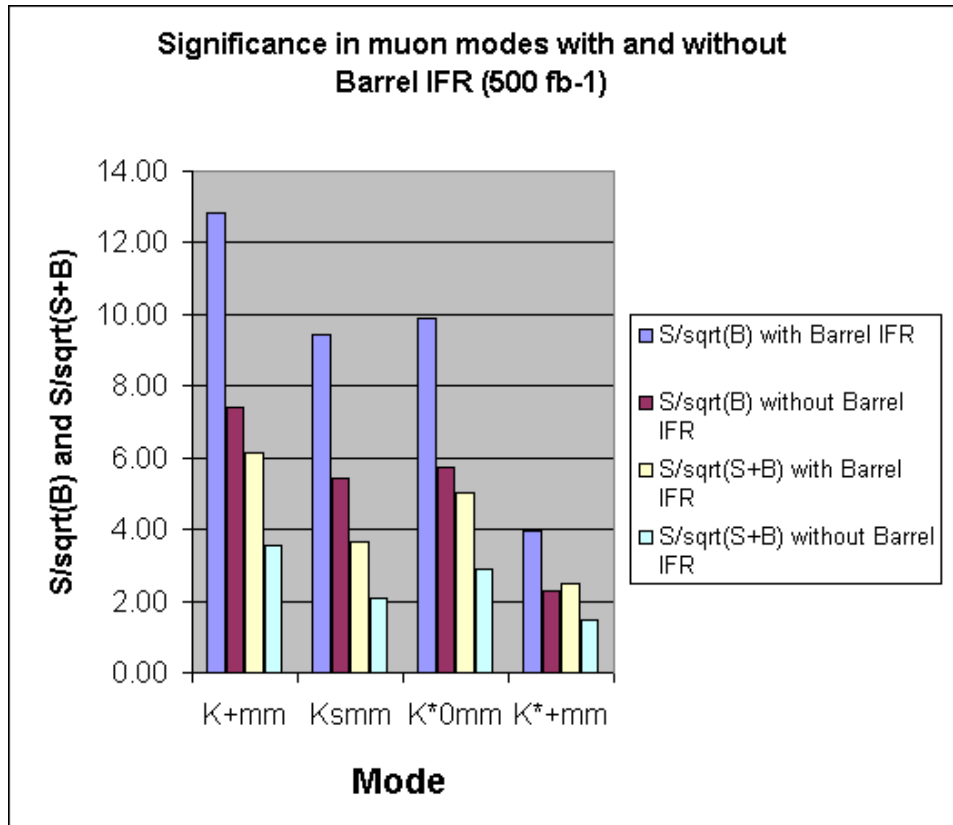


Figure 7: Significance measures S/\sqrt{B} and $S/\sqrt{S+B}$ for $B \rightarrow K^{(*)}\mu^+\mu^-$ modes with and without the IFR barrel upgrade.

decays is itself a broad physics program involving many different modes and techniques. Due to the small branching fractions, all of these measurements currently have large statistical errors. Currently, the theoretical uncertainties are also large, a point we will return to below.

In $b \rightarrow u\ell^-\bar{\nu}$ decays, the rates to the electron and muon channels are nearly identical (although there are radiative effects in electron events that must be taken into account). Typically, the muon samples provide somewhat less than half the total signal events, since the minimum momentum cutoff for muons is higher than that for electrons. The comparison between electron and muon results provides a valuable cross check on the measurements.

The challenge of $|V_{ub}|$ measurements is to extract clean signals while at the same time keeping the dependence on theoretical models to a minimum. Typically, there exist kinematic regions in which theoretical predictions are most reliable; restricting the event sample to such regions reduces the theoretical errors but increases the statistical uncertainties. For example, lattice calculations for $B \rightarrow \pi\ell^-\bar{\nu}$ are steadily improving, but they are most reliable at high q^2 , where the decay rate goes to zero. Thus, we would like to restrict the sample to a high q^2 region, and this will require very large event samples.

In *BABAR* we are pursuing both inclusive and exclusive methods for measuring $|V_{ub}|$. The inclusive result, which has been presented at the Moriond 2003 Conference, is particularly interesting because it uses a new and powerful technique. The study uses the hadronic B_{reco} sample, that is, the event sample in which one of the B mesons is fully reconstructed in a hadronic final state. Although the total event sample is greatly reduced, there is also a large reduction in combinatoric background. This technique allows an estimate of the mass of the hadronic system X produced in semileptonic B decay, and the requirement $M(X) < M(D)$ greatly suppresses the $b \rightarrow c\ell^-\bar{\nu}$ background. Both electron and muon channels are used, with muons being identified with “very tight” criteria. A particularly interesting feature of this approach is that the continuum background, which can be very large in other inclusive measurements at the $\Upsilon(4S)$, is highly suppressed by the requirement of a fully reconstructed B meson.

Figure 8 shows the hadronic recoil mass m_X , in which the $B \rightarrow X_u\ell^-\bar{\nu}$ signal peaks below m_D . Figure 9 shows a comparison of the $B \rightarrow X_u\ell^-\bar{\nu}$ branching fraction (relative to that for $B \rightarrow X_c\ell^-\bar{\nu}$) in several subsamples. The separate electron and muon results are shown. In a sample of 82 fb^{-1} there are 88 ± 16 $B \rightarrow X_u e\bar{\nu}$ events and 69 ± 16 $B \rightarrow X_u \mu\bar{\nu}$ events. Thus, assuming the same efficiencies, an $\Upsilon(4S)$ data sample of 500 fb^{-1} would yield 537 events in the electron channel and 421 events in the muon chan-

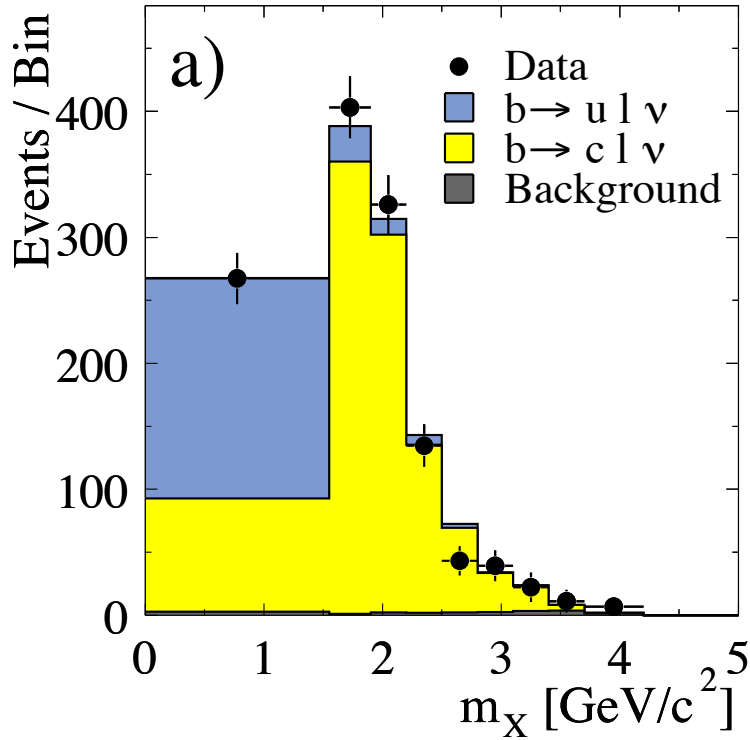


Figure 8: *BABAR* measurement of the inclusive $B \rightarrow X_u \ell^- \bar{\nu}$ branching fraction. The plot shows the distribution of the hadronic recoil mass m_X . The signal is contained largely in the single bin below the D mass. The rest of the events are dominated by $b \rightarrow c \ell^- \bar{\nu}$ background. Measurements of inclusive and exclusive $B \rightarrow X_u \ell^- \bar{\nu}$ decays, which are used to extract $|V_{ub}|$, are an important part of *BABAR*'s long term physics program.

nel. Without the barrel IFR replacement, the muon yield would fall to 210 events. These muon yields are conservative, since they are based on the time-averaged efficiencies in the real IFR system, which should have lower efficiency than a replacement system..

Measurements of exclusive modes would be similarly affected if the barrel is not replaced. The decay $B \rightarrow \pi \ell^- \bar{\nu}$ is an important example: according to lattice theorists [3], reducing many of the theoretical uncertainties is mainly a matter of getting more computer time. In a current *BABAR* analysis [4], which is in preliminary form, the signal efficiency is around 1%, and in a

$R_{u/sl}$ enriched sample

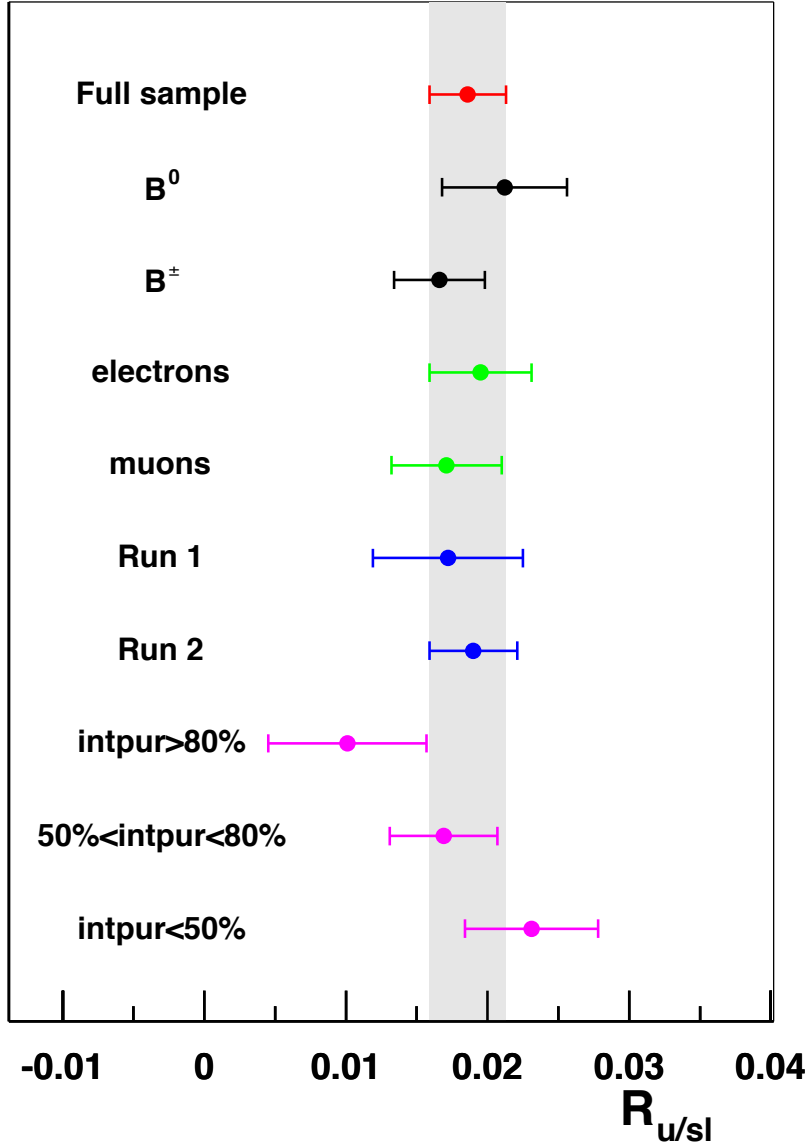


Figure 9: Cross checks within the *BABAR* measurement of the inclusive $B \rightarrow X_u \ell^- \bar{\nu}$ branching fraction. The quantity plotted is $R_{u/sl} = \mathcal{B}(B \rightarrow X_u \ell \nu) / \mathcal{B}(B \rightarrow X \ell \nu)$. Separate electron and muon results are shown. Both the electron and muon channels contribute significantly to the result.

500 fb⁻¹ sample, the $B \rightarrow \pi^- \mu^- \bar{\nu}$ signal yield would be around 990 events. Without the IFR barrel replacement, the yield would be about 500 events. This method is based on the neutrino reconstruction method invented in CLEO, and it results in a relatively low level of continuum background.

With large data samples, we can study the kinematic distributions of these decays, which will help to test theoretical predictions. A precise measurement of the q^2 spectra for $B \rightarrow \pi(\rho)\ell^- \bar{\nu}$ is a long-term goal. In addition, several new exclusive modes will become accessible, such as $B \rightarrow \omega \ell^- \bar{\nu}$ and $B \rightarrow \eta \ell^- \bar{\nu}$. For all of these reasons, we expect the study of both inclusive and exclusive $b \rightarrow u \ell^- \bar{\nu}$ processes to be a key part of the *BABAR* physics program for the long-term future.

The $B \rightarrow X_u \ell^- \bar{\nu}$ analysis described above is an interesting test case for using the EMC and IFR to veto background with K_L^0 mesons. Since part of the $b \rightarrow c \ell^- \bar{\nu}$ background suppression is achieved by vetoing events in which the non- B_{reco} part of the event has a kaon, any mechanism by which charged or neutral kaons escape detection results in a larger background. However, present studies [5] indicate that only about one-quarter of the $b \rightarrow c \ell^- \bar{\nu}$ background that enters the region $M(X) < 1.6$ GeV is associated with undetected K_L^0 's. Additional cuts may eventually increase this fraction, but it does not appear that a K_L^0 veto will make a large difference to the analysis.

3.4.3 Lepton tagging for CP asymmetry measurements

We have studied the impact of the loss of muon efficiency on tagging for CP analyses. If muons are removed from tagging, they tend to be recovered in redundant categories, so that the statistical effect is minor [6]. However, CP asymmetry measurements with large event samples, such as $\sin 2\beta$ in $B \rightarrow J/\psi K_S^0$, are known to be sensitive to tag-side CP violation. In such cases, the lepton tags are preferred and muon identification will be important.

3.5 Characteristics of the current IFR barrel

We now briefly review aspects of the IFR barrel that relate to its performance in physics measurements. In particular, we discuss the overall detector geometry and the configuration of the absorber. In this discussion, it is useful to remember that 90° in the CM frame corresponds to 61° in the lab frame, or $\cos \theta_{\text{lab}} = +0.48$, rather than $\cos \theta_{\text{lab}} = 0$.

Figure 10 shows the amount of material traversed by a high-momentum track before reaching the first active layer of the IFR (layer 1). The total

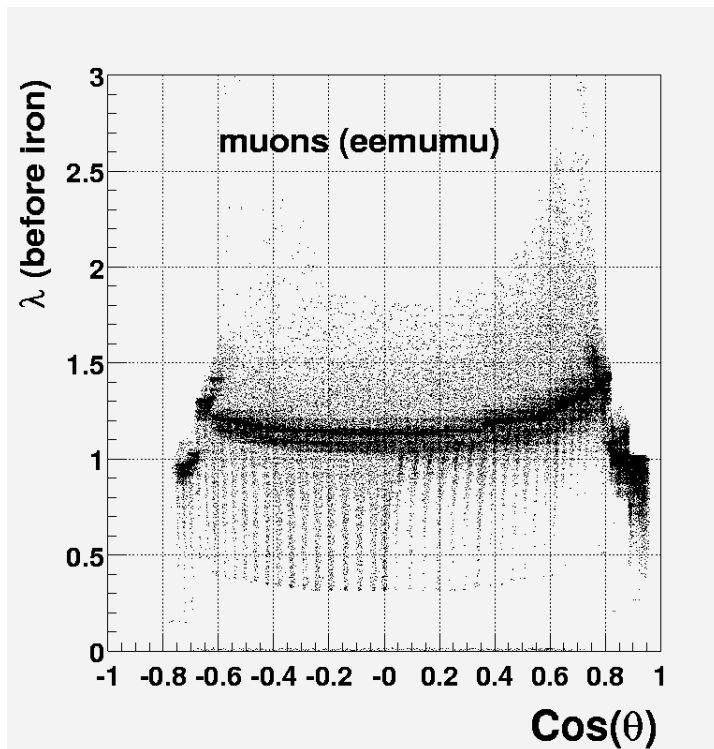


Figure 10: Map of the amount of material (expressed in nuclear interaction lengths) that a track is expected to encounter before entering the first active detector layer of the IFR. This quantity is computed with the track swimmer and detector model used in event reconstruction.

is roughly 1.0–1.3 nuclear interaction lengths, a large part of which is from the CsI calorimeter crystals and the magnet coil. Assuming a typical value of $1.2 \lambda_{\text{int}}$ and using a value of 16.8 cm for the interaction length of iron, the material in front of the IFR is equivalent to about 20.2 cm of iron.

The IFR barrel comprises 19 detector layers, which alternate with layers of iron absorber of varying thickness. Table 3 lists the detector and absorber layers. One of the most prominent features of the absorber design is the high degree of longitudinal segmentation in layers 1–10. Between these layers, the iron absorber is only 2 cm ($0.12 \lambda_{\text{int}}$) thick. The purpose of this fine segmentation was to maximize the efficiency for K_L^0 detection in $B^0 \rightarrow J/\psi K_L^0$. Since this goal is less important now than it was in the early phase of *BABAR*, it is appropriate to revisit the configuration of the absorber.

Within the IFR barrel itself, there are 65 cm of iron before layer 19. This

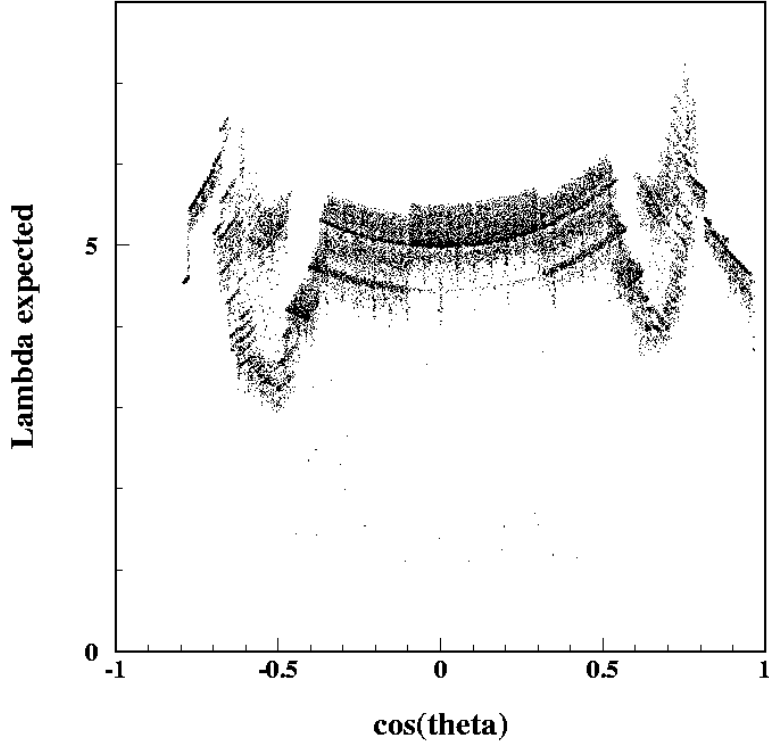


Figure 11: Material map for the original IFR, which was used for Runs 1 and 2. Before Run 3, the IFR forward endcap chambers were replaced and the absorber configuration was changed.

corresponds to $3.9 \lambda_{\text{int}}$. Including the material in front of the IFR, the total is about $5.1 \lambda_{\text{int}}$. The largest increments in material are within the last few layers, as shown in Table 3.

Figure 11 shows the amount of material (as computed by the swimmer) that is traversed by a high-momentum track before reaching the outermost layer of the IFR. In this plot, it is assumed that all chambers are fully efficient. However, the geometrical acceptance is taken into account, and this has a large effect for layer 19, which only has partial coverage due to the complex array of services that are mounted on the outside of the barrel. (Layer 19 is also completely inaccessible, a point we will return to below.) From this plot, we see that the total amount of material in the existing configuration is a complicated function of $\cos\theta$. The total amount of material in the barrel region has a median value of about 5.1 interaction

Table 3: Current configuration of IFR barrel layers.

Layer	Det/Absorb	Absorb. Thick. (cm)	Cum. Absorber (cm)	Absorber Increment (λ_{int})	Cum. Absorber (λ_{int})
	Before L1	20.2	20.2	1.20	1.20
1	Det				
	Fe	2	22.2	0.12	1.32
2	Det				
	Fe	2	24.2	0.12	1.44
3	Det				
	Fe	2	26.2	0.12	1.56
4	Det				
	Fe	2	28.2	0.12	1.68
5	Det				
	Fe	2	30.2	0.12	1.80
6	Det				
	Fe	2	32.2	0.12	1.91
7	Det				
	Fe	2	34.2	0.12	2.03
8	Det				
	Fe	2	36.2	0.12	2.15
9	Det				
	Fe	2	38.2	0.12	2.27
10	Det				
	Fe	3	41.2	0.18	2.45
11	Det				
	Fe	3	44.2	0.18	2.63
12	Det				
	Fe	3	47.2	0.18	2.81
13	Det				
	Fe	3	50.2	0.18	2.99
14	Det				
	Fe	5	55.2	0.30	3.28
15	Det				
	Fe	5	60.2	0.30	3.58
16	Det				
	Fe	5	65.2	0.30	3.88
17	Det				
	Fe	10	75.2	0.60	4.47
18	Det				
	Fe	10	85.2	0.60	5.07
19	Det				

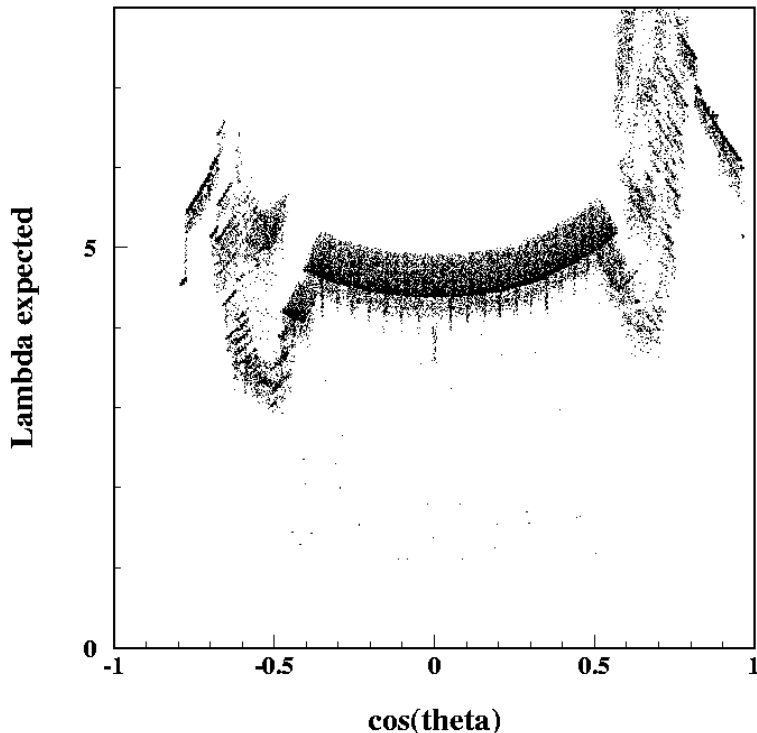


Figure 12: Material map for the IFR with the new forward endcap and barrel layer 19 no longer functioning.

lengths at 90° to the beam axis.

There is also φ dependence, which is not explicitly shown in this plot. The detector/absorber layers are arranged in six sextants. Since the layers are planar, rather than cylindrical, the amount of material encountered depends on φ as well as $\cos\theta$. The effect of the gaps between the sextants is discussed below.

Because the detectors in barrel layer 19 are inaccessible, it will not be possible to replace them, and the 10 cm of Fe (about $0.6 \lambda_{\text{int}}$) immediately in front of layer 19 will be effectively lost as far as physics performance is concerned. Figure 12 shows the number of interaction lengths traversed by high-momentum muons when layer 19 is removed. This figure also incorporates the design of the new forward endcap, which was installed in summer 2002, prior to Run 3. The plot therefore shows the amount of useful ab-

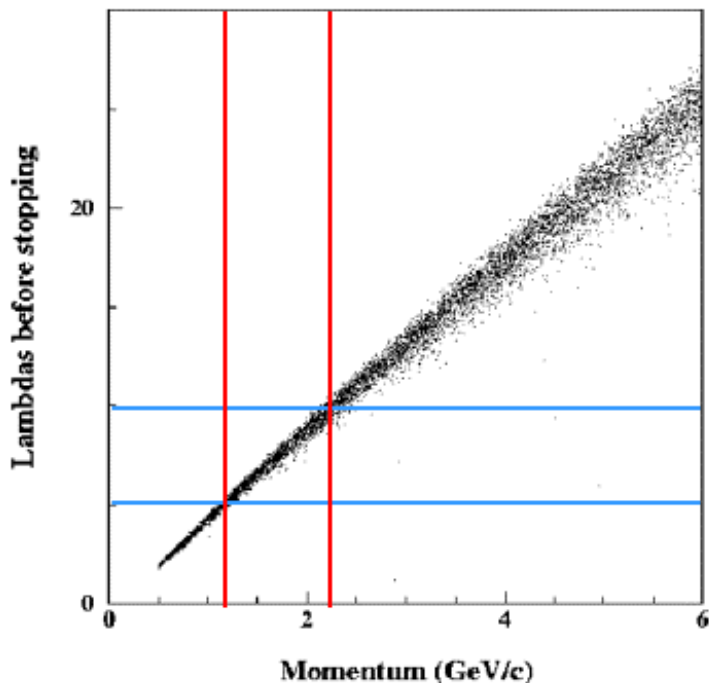


Figure 13: GEANT Monte Carlo simulation for muon range as a function of momentum. The horizontal blue lines are drawn at 5 and 10 interaction lengths.

sorber in the detector for the future, if we did not reconfigure the absorber in the barrel region. In this scenario the total amount of material in the barrel region is typically below five interaction lengths.

This amount of material is at the lower end of what is desirable for a muon ID system for the $\Upsilon(4S)$ energy range. In the CLEO experiment, for example, there are $7\lambda_{\text{int}}$ at normal incidence. Muon chambers are placed after 3, 5, and 7 interaction lengths. Although most CLEO analyses involving muons do not require penetration through the full absorber thickness, requiring full penetration is very valuable in certain analyses where pions faking muons are a severe background.

In general, the amount of useful iron absorber is closely related to the momentum spectrum of the muons being identified. Higher momentum muons will traverse more material, and this can be used to discriminate against hadrons, which will have a higher probability to interact if there is more material. For reference, we have included some basic plots that relate

to this question. Figure 13 shows a simple GEANT-based simulation for muon range in iron (expressed in interaction lengths) as a function of muon momentum. The relationship is essentially linear and can be summarized (to one significant figure!) by

$$\frac{L}{\lambda_{\text{int}}} \approx 5 \cdot \frac{p}{1 \text{ GeV}/c} \quad (3)$$

The horizontal lines in the figure correspond to 5 and 10 interaction lengths, respectively. We see that muons of momentum around $1.2 \text{ GeV}/c$ will traverse 5 interaction lengths; muons of $2 \text{ GeV}/c$ will traverse nearly 10 interaction lengths before stopping.

In *BABAR* muon selectors, the effective cut on the number of interaction lengths is related to the momentum of the track. Although a $1 \text{ GeV}/c$ muon will traverse only five interaction lengths, higher momentum muons will go further, and this requirement can be applied on a track-by-track basis to obtain the best performance.

As an example, Fig. 14 shows the muon spectrum from inclusive $B \rightarrow X_u \ell^- \bar{\nu}$, shown not as a distribution in momentum, but instead in the number of interaction lengths traversed. The tracks shown are in the pure barrel region. It is clear that a large fraction of the muons traverse more than five interaction lengths. In fact, a large fraction of muons will go all the way through the IFR.

Due to the boost from the CM frame to the lab frame, there is a significant correlation between lab-frame polar angle and lab-frame momentum. Figure 15 shows the same distribution for tracks in the overlap region between the barrel and the forward endcap. Muons in the forward region have an even larger range, but there is also more material there.

Figure 16 shows the probability that pions will not interact within a given number of interaction lengths. The momentum dependence is mild and the probabilities at the plateaus follow an $\exp(-x/\lambda_{\text{int}})$ behavior. Note that a pion that interacts can sometimes be identified as a muon, so this plot is not the same as the pion fake probability. However, it gives a rough idea of the limiting performance of an absorber system.

Before considering alternative absorber layouts, we note one last feature of the barrel IFR. As we discussed earlier, the IFR barrel is segmented into six azimuthal sectors, called sextants. The gaps between these sextants are substantial, and they result in a loss of geometric acceptance of about 8%. Figure 17 shows the efficiency as a function of a “folded” φ variable that combines all six sextants into one plot. The *BABAR* tight muon selector is used.

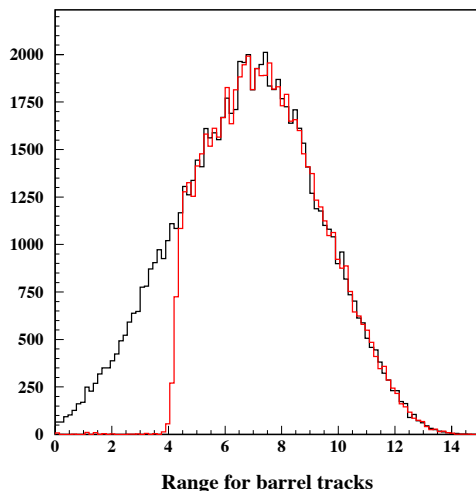


Figure 14: Distribution of expected muon ranges, expressed in nuclear interaction lengths, for muons from inclusive $B \rightarrow X_u \ell^- \bar{\nu}$ decay. Because momentum in the lab frame is highly correlated with polar angle, we have selected the IFR pure barrel region only for this figure. The red histogram corresponds to muons with momenta greater than $1 \text{ GeV}/c$. A large fraction of muons from this process travel all the way through the IFR. This is true for many other processes as well.

3.6 Simulation of Benchmark Designs

The replacement of the IFR barrel detector modules provides an opportunity to improve the configuration of the absorber. As we have discussed, the number of interaction lengths in the current IFR barrel is low for a detector operating at the $\Upsilon(4S)$, and the effective loss of 10 cm of iron in front of layer 19 will make the problem even worse.

To examine this question, we have constructed three benchmark designs: BD1, BD2, and BD3. These designs replace some of the active detector layers in the barrel with brass plates 2.2 cm thick. A similar change has already been made for the forward endcap.

Tables 4, 5, and 6 show the absorber layouts for our three benchmark configurations. BD1 is similar to the new layout in the forward endcap. It has brass absorber added to five intermediate layers: 8, 10, 12, 14, and 16. In BD2, six absorber layers are added, but they are installed in layers that

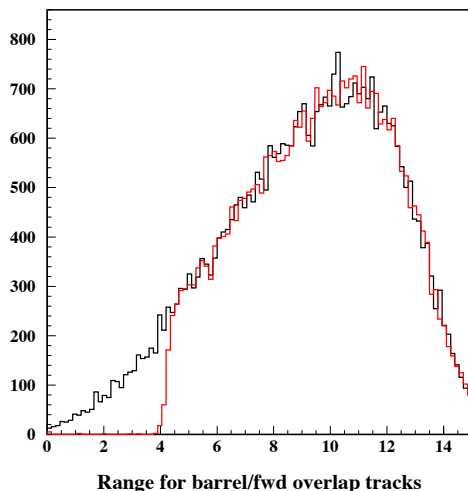


Figure 15: Distribution of expected muon ranges, expressed in nuclear interaction lengths, for muons from inclusive $B \rightarrow X_u \ell^- \bar{\nu}$ decay. This figure shows muons in the barrel-endcap overlap region, where the typical momentum is higher than in the pure barrel region. The red histogram corresponds to muons with momenta greater than $1 \text{ GeV}/c$.

are closer to the front: 5, 7, 9, 11, 13, and 15. This design has a greater emphasis on muon ID at the expense of some K_L^0 efficiency. Both BD1 and BD2 have just over 5 interaction lengths total. The BD3 design is more ambitious, with 9 layers of brass added. This design is heavily weighted toward muon identification, and it would compromise K_L^0 efficiency. Although we have studied BD3, it was clear from the start that it is not a realistic design, because the total mass added to the detector is not compatible with earthquake safety constraints. As described in the next chapter, BD1 and BD2 do satisfy these constraints.

The absorber designs are driven by several basic principles. First, for robustness, the extra absorber should not be installed in the outer layers, because it is important that there be a sufficient number of detector layers beyond the absorber layers to ensure high efficiency. One of the difficulties in the current system is that the failure of chambers in the outer layers results in a large reduction in the amount of useful material. In addition, a given thickness of material is significantly heavier if it is installed in the

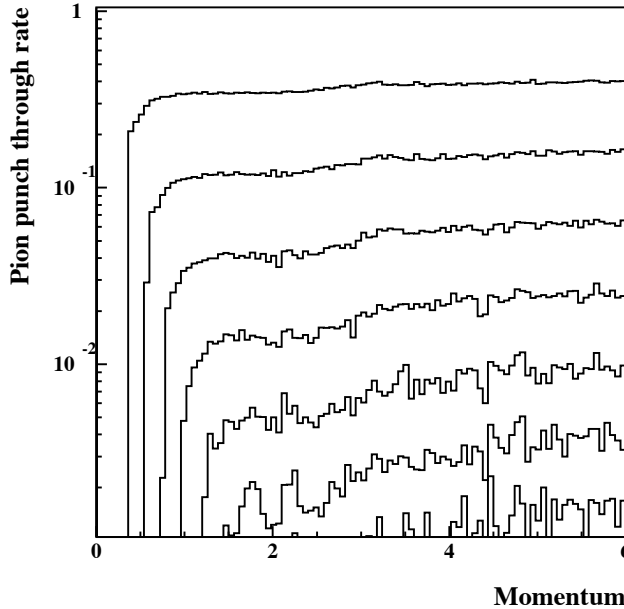


Figure 16: GEANT simulation of the probability for a muon to penetrate N interaction lengths without interacting, for $N = 1$ (upper curve) to $N = 7$ (lower curve).

outer layers. In fact, the barrel already has its thickest absorber layers at large radii.

In BD2, we have attempted to make the absorber thickness reasonably uniform between the detectors. If we consider an absorber layer with $\lambda_{\text{int}} = 0.4$, this gives a pion reduction of about 0.67 and a muon energy loss of about $\Delta E = 80 \text{ MeV}$. Compared to the typical widths of the muon momentum spectra of interest, this is a reasonably small energy interval. The absence of further detector/absorber segmentation within this ΔE interval means that within this narrow range π rejection is in principle suboptimal. Certainly the segmentation of $\lambda_{\text{int}} = 0.12$ in the layers 1–10 of the current IFR barrel is not needed for muon identification. Although the absorber thicknesses in BD2 are not constant, they are all in the range 0.3–0.6 λ_{int} except in the inner layers, where we have retained a smaller segmentation for K_L^0 identification and to keep the mass down.

In all benchmark designs we have retained detectors in layer 1 for linking with the tracking system.

Figure 18 shows the material maps for each of the benchmark designs

Table 4: Configuration of Benchmark Design #1 (BD1). Note the absence of layer 19. In five layers (8, 10, 12, 14, and 16), the detectors have been replaced by 2.2 cm-thick brass plates.

Layer	Det/Absorb	Absorb.Thick (cm Fe equiv.)	Cum. Absorber (cm Fe equiv.)	Absorber Increment (λ_{int})	Cum. Absorber (λ_{int})
	Before L1	20.2	20.2	1.20	1.20
1	Det				
	Fe	2.0	22.2	0.12	1.32
2	Det				
	Fe	2.0	24.2	0.12	1.44
3	Det				
	Fe	2.0	26.2	0.12	1.56
4	Det				
	Fe	2.0	28.2	0.12	1.68
5	Det				
	Fe	2.0	30.2	0.12	1.80
6	Det				
	Fe	2.0	32.2	0.12	1.92
7	Det				
	Fe	2.0	34.2	0.12	2.04
8	Brass	2.3	36.5	0.14	2.17
	Fe	2.0	38.5	0.12	2.29
9	Det				
	Fe	2.0	40.5	0.12	2.41
10	Brass	2.3	42.8	0.14	
	Fe	3.0	45.8	0.18	2.55
11	Det				2.73
	Fe	3.0	48.8	0.18	2.91
12	Brass	2.3	51.1	0.14	3.04
	Fe	3.0	54.1	0.18	3.22
13	Det				
	Fe	3.0	57.1	0.18	3.40
14	Brass	2.3	59.4	0.14	3.54
	Fe	5.0	64.4	0.30	3.84
15	Det				
	Fe	5.0	69.4	0.30	4.13
16	Brass	2.3	71.7	0.14	4.27
	Fe	5.0	76.7	0.30	4.57
17	Det				
	Fe	10.0	86.7	0.60	5.16
18	Det				

Table 5: Configuration of Benchmark Design #2 (BD2). Note the absence of layer 19. In six layers (5, 7, 9, 11, 13, and 15), the detectors have been replaced by 2.2 cm-thick brass plates.

Layer	Det/Absorb	Absorb.Thick (cm Fe equiv.)	Cum. Absorber (cm Fe equiv.)	Absorber Increment (λ_{int})	Cum. Absorber (λ_{int})
	Before L1	20.2	20.2	1.20	1.20
1	Det				
	Fe	2.0	22.2	0.12	1.32
2	Det				
	Fe	2.0	24.2	0.12	1.44
3	Det				
	Fe	2.0	26.2	0.12	1.56
4	Det				
	Fe	2.0	28.2	0.12	1.68
5	Brass	2.3	30.5	0.14	1.82
	Fe	2.0	32.5	0.12	1.94
6	Det				
	Fe	2.0	34.5	0.12	2.05
7	Brass	2.3	36.8	0.14	2.19
	Fe	2.0	38.8	0.12	2.31
8	Det				
	Fe	2.0	40.8	0.12	2.43
9	Brass	2.3	43.1	0.14	2.57
	Fe	2.0	45.1	0.12	2.69
10	Det				
	Fe	3.0	48.1	0.18	2.86
11	Brass	2.3	50.4	0.14	3.00
	Fe	3.0	53.4	0.18	3.18
12	Det				
	Fe	3.0	56.4	0.18	3.36
13	Brass	2.3	58.7	0.14	3.50
	Fe	3.0	61.7	0.18	3.68
14	Det				
	Fe	5.0	66.7	0.30	3.97
15	Brass	2.3	69.1	0.14	4.11
	Fe	5.0	74.1	0.30	4.41
16	Det				
	Fe	5.0	79.1	0.30	4.71
17	Det				
	Fe	10.0	89.1	0.60	5.30
18	Det				

Table 6: Configuration of Benchmark Design #3 (BD3). Note the absence of layer 19. In nine layers (2, 3, 4, 5, 7, 9, 11, 13, and 15), the detectors have been replaced by 2.2 cm-thick brass plates.

Layer	Det/Absorb	Absorb.Thick (cm Fe equiv.)	Cum. Absorber (cm Fe equiv.)	Absorber Increment (λ_{int})	Cum. Absorber (λ_{int})
	Before L1	20.2	20.2	1.20	1.20
1	Det				
	Fe	2.0	22.2	0.12	1.32
2	Brass	2.3	24.5	0.14	1.46
	Fe	2.0	26.5	0.12	1.58
3	Brass	2.3	28.8	0.14	1.71
	Fe	2.0	30.8	0.12	1.83
4	Brass	2.3	33.1	0.14	1.97
	Fe	2.0	35.1	0.12	2.09
5	Brass	2.3	37.4	0.14	2.23
	Fe	2.0	39.4	0.12	2.35
6	Det				
	Fe	2.0	41.4	0.12	2.46
7	Brass	2.3	43.7	0.14	2.60
	Fe	2.0	45.7	0.12	2.72
8	Det				
	Fe	2.0	47.7	0.12	2.84
9	Brass	2.3	50.0	0.14	2.98
	Fe	2.0	52.0	0.12	3.10
10	Det				
	Fe	3.0	55.0	0.18	3.27
11	Brass	2.3	57.3	0.14	3.41
	Fe	3.0	60.3	0.18	3.59
12	Det				
	Fe	3.0	63.3	0.18	3.77
13	Brass	2.3	65.6	0.14	3.90
	Fe	3.0	68.6	0.18	4.08
14	Det				
	Fe	5.0	73.6	0.30	4.38
15	Brass	2.3	75.9	0.14	4.52
	Fe	5.0	80.9	0.30	4.82
16	Det				
	Fe	5.0	85.9	0.30	5.11
17	Det				
	Fe	10.0	95.9	0.60	5.71
18	Det				

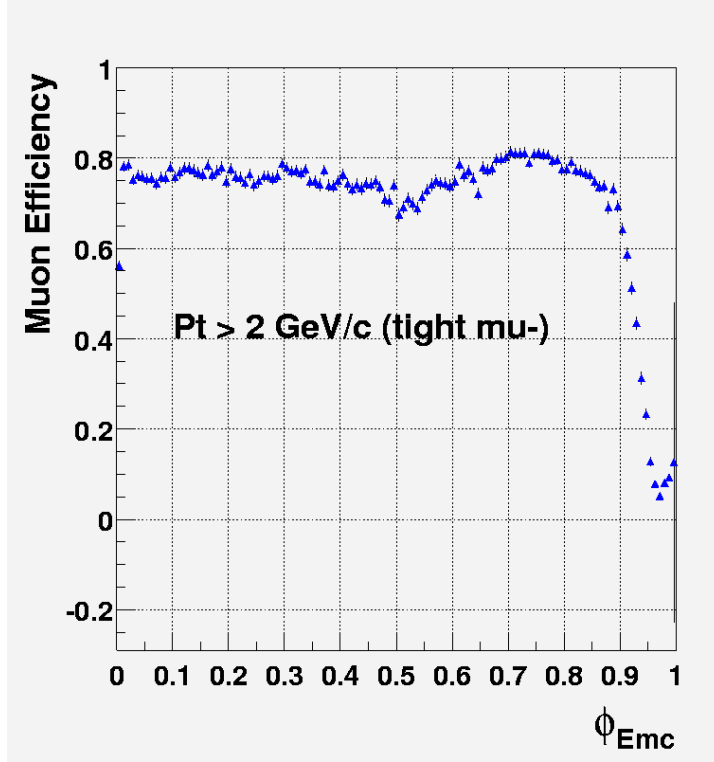


Figure 17: The barrel IFR muon efficiency as a function of the folded φ variable, which superimposes all six sextants. The loss of efficiency due to the cracks between the sextants integrates to about 8%.

and for the original IFR barrel.

Figure 19 shows a GEANT-based comparison of the performance of different IFR barrel configurations. The tracks are muons and pions with momenta greater than $2 \text{ GeV}/c$ in the pure barrel region only ($1 < \theta < 2$ rad). The curves on this plot are based on a neural-net selector that uses only the information on track penetration distance. We call this a “simple selector” because it is based on minimal information related only to the distribution of material through the detector. Two quantities are used: the number of interaction lengths traversed and the difference between the expected and actual number of interaction lengths traversed. The effect of other quantities, such as the χ^2 of the match of the extrapolated track to the IFR hits, is discussed below. For each detector configuration, the simple selector produces a curve that gives the probability for a pion to fake a muon

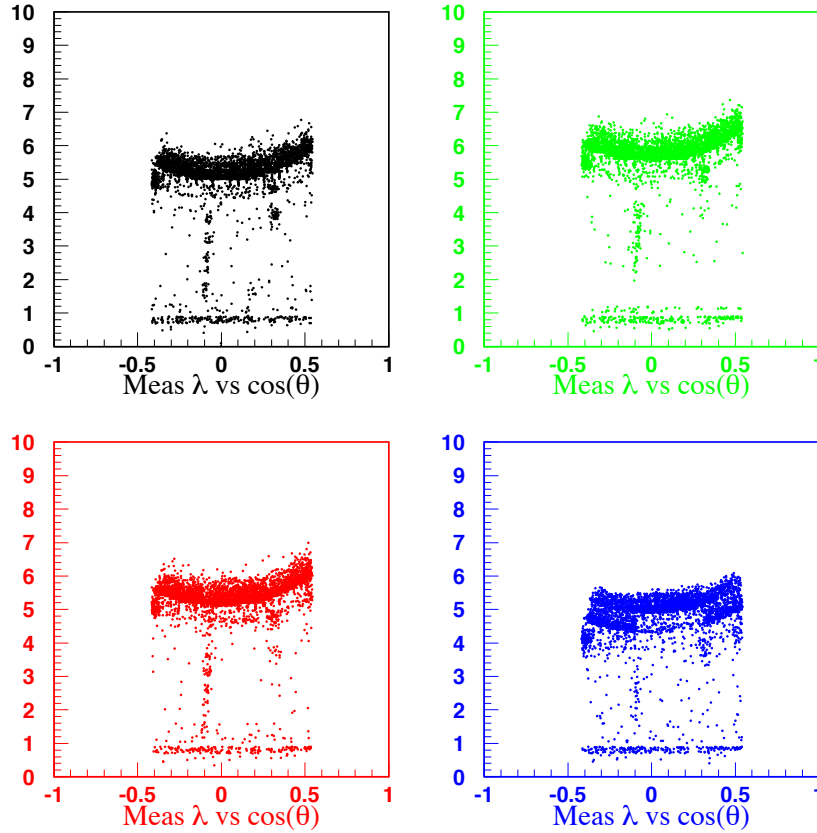


Figure 18: Number of interaction lengths vs. $\cos\theta$ for BD1 (black, upper left), BD2 (red, lower left), BD3 (green, upper right), and the current detector (blue, lower right). The material is mapped with the track swimmer and detector model used in the reconstruction.

as a function of the muon detection efficiency. In this plot, the region at the lower right corresponds to the best performance.

The three lower curves in Fig. 19 show the performance of the benchmark designs. The layout with the best muon performance is BD3, which is not surprising because it has the most material. BD1 and BD2 have similar behavior to each other, with BD2 performing slightly better. This is expected because BD2 has one more layer of absorber than BD1. In all of

these curves, the detectors are assumed to have the same active area as the installed RPC chambers and to be 95% efficient over their area.

Besides the benchmark designs, Fig. 19 shows four other curves. The curve above the three benchmark curves shows the “Nominal” IFR, which we define to be the original IFR barrel, including layer 19. The RPC efficiencies have been set at 95%, the same value used for the benchmark designs. We see that all benchmark designs perform better than this idealized original detector. The fifth curve from the bottom (“Initial”) is also based on the original IFR barrel design, including layer 19. In this case, however, detector efficiencies from February 2000 are used instead of the 95% efficiencies.

Finally, we examine the top two curves in Fig. 19. The “Nolayer19” curve is the same as “Nominal,” but has no layer 19. This means that the detector and absorber layout is that of the installed IFR, except that the chamber efficiencies are 95% and layer 19 is removed. The reason for studying this configuration is that it corresponds to what we would get if we simply replace the barrel RPCs with chambers that are 95% efficient, except for layer 19, which is inaccessible. The difference between the Nolayer19 curve and the benchmark design curves shows the improvement from modifying the absorber. The gain is roughly a factor of two in pion rejection at a fixed muon efficiency.

The curve “June2002,” which shows the worst performance, corresponds to the installed system with detector efficiencies as of June 2002. Layer 19 is included, but many of the detectors have low efficiencies.

The performance of all of the detector designs is enhanced by using additional information beyond track penetration distance. Figure 20 shows that by using additional variables in the neural net selector, we can reduce the pion misidentification probability by about a factor of two. For example, at a muon efficiency of 70%, we can reduce the pion fake rate from 5.3% to 2.2%. These curves are based on control samples from data taken in 2000.

The K_L^0 efficiencies of the benchmark designs have also been studied. As expected, BD3 has very poor K_L^0 efficiency. For a two layer cluster, the K_L^0 efficiency is only 9%. For BD1 and BD2, the K_L^0 efficiencies are 30% and 28%. If we use the absorber configuration of the current detector, but assume 95% RPC efficiencies (much higher than actual), then the K_L^0 efficiency would be 35%. (We note that about half of the K_L^0 ’s are detected in the CsI calorimeter.) Thus, BD1 and BD2 are both similar in K_L^0 performance to the current configuration.

Finally, we can make a rough estimate of how long it will take for the new data from the IFR replacement to make up (statistically) for the lost electron data that one would have acquired during the installation time.

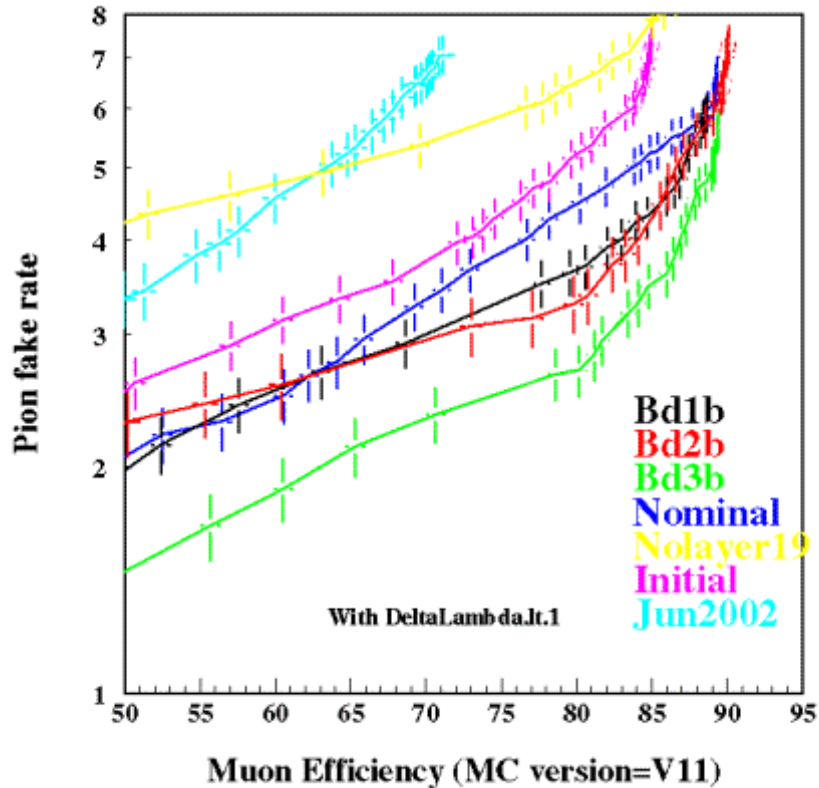


Figure 19: Performance of various IFR barrel configurations in terms of muon efficiency and pion rejection. The curves are discussed in detail in the text.

The installation will overlap a normal shutdown, so the accelerator would be off for much of the time anyway. We consider an analysis for which the muon to electron yields are in the ratio $\mu/e = 3/4$ and use the fact that the barrel represents half of the muon acceptance. If an additional month is required for the IFR installation beyond what is needed for accelerator work, then the statistical loss of electron data will be more than made up after four months.

3.7 Conclusions

There is a compelling physics case for an IFR barrel upgrade. In particular,

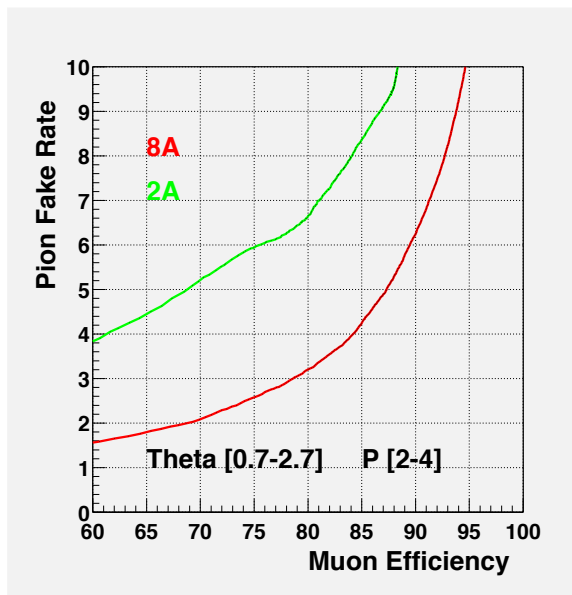


Figure 20: Improvement in muon identification/pion rejection from additional discriminating variables besides λ_{int} and $\Delta\lambda_{\text{int}}$. Six additional variables are used, including the χ^2 of the extrapolated track with respect to the IFR hits. The muons are from an $e^+e^- \rightarrow e^+e^-\mu^+\mu^-$ sample and the pions are from $\tau^+\tau^-$ 1 vs. 3 prong events. The additional variables give about a factor of two improvement in the pion rejection at a fixed muon efficiency. The data are from the 2000 run.

1. The decline in the efficiencies of the Resistive Plate Chambers (RPCs) in the IFR has already had, and will continue to have, a significant negative impact on many *BABAR* physics analyses that require muon identification.
2. Muon identification is required for a large number of processes that we will continue to study in the future, including several measurements that are central to the *BABAR* physics program. These include measurements of $|V_{ub}|$ and electroweak penguin decays. Without a high quality muon system, *BABAR* will be at a significant disadvantage compared with Belle and, in certain measurements, with CDF.
3. The barrel IFR represents about half of our muon acceptance. Studies of modes with two muons in the final state, such as $B \rightarrow K^*\mu^+\mu^-$, will be severely affected if the IFR barrel chambers are not replaced.

4. The amount of hadron absorber in the current IFR is at the low end of what is desirable for a muon system. The problem is exacerbated by the loss of efficiency in layer 19 detectors, which effectively removes 10 cm of iron.
5. We can significantly improve the performance of the IFR for muon identification by replacing some of the active detector layers with absorber. We have considered three benchmark designs (BD1, BD2, BD3) under the assumption that the detector efficiencies are 95%. Although BD3 has the best performance for muon identification, it is excluded by weight considerations. Both BD1 and BD2 are reasonable designs, with BD2 having the edge since it has 6 absorber layers rather than 5. By a reasonable design, we mean that
 - (a) There are some active layers near the front of the IFR barrel to preserve K_L^0 efficiency and track linking to the drift chamber.
 - (b) The absorber layers are not concentrated at the back, where they would come after many of the detector layers. Such designs would be more sensitive to the loss of efficiency in detectors in the outer layers, a problem that we are currently having.
 - (c) The spacing, $\Delta\lambda_{\text{int}}$, between detector layers is around 0.4–0.6 except in the inner layers, which are used for K_L^0 identification.

Of these benchmark designs, BD2 is the preferred configuration.

6. Installation time for the IFR should be kept to a minimum through careful planning and design. If this can be done, the added data from the IFR will far outweigh the loss of electron data resulting from the down time associated with installation.

References

- [1] BaBar Collaboration, hep-ex/0207082 (BAD #466) (2002); A. Samuel *et al.*, BAD #341 (2002).
- [2] J. Berryhill, IFR workshop, Nov. 14–15, 2002, <http://www.slac.stanford.edu/BFROOT/www/Detector/IFR/IfrUpgradeReview2002/021114Workshop/16.Berryhill.pdf>.
- [3] A.X. El-Khadra *et al.*, Phys. Rev. D **64**, 014502 (2001).

- [4] A. Weinstein, *BABAR* V_{xb} workshop, December 4–6, 2002, <http://www.slac.stanford.edu/www/Physics/workshops/vxb2002>.
- [5] A. Sarti, D. del Re, R. Faccini, U. Langenegger, *BABAR* analysis document #540 (2003).
- [6] G. Sciolla, Sin2beta hypernews posting 488.1 (2002).

4 Common Engineering Issues

4.1 Description of the Flux Return and Limitations to Access

The Barrel IFR is divided into six sections in azimuth (Fig. 21). Each section consists of two side plates that extend along the beam line and are perpendicular to it, and 18 sheets of steel graded in thickness between 1 and 5 inches as their distance increases from the beam line. These steel plates are welded to the side plates longitudinally. The gap between plates contains the sensor elements, monolithic RPCs. During manufacture and assembly of the steel, a gauge was passed through the gap assuring that the gap is everywhere at least 22mm. The gaps between plates are larger at the ends. The six sections are bolted together. They are suspended from a pair of circumferential beams that are cradled on four legs that rest on earthquake isolators. Layer 19, which provides partial coverage of the barrel, is trapped between the 18th layer of steel and these beams.

The structure is complicated by the need to provide a return path for the magnetic flux. The proximity of the floor to the bottom sextant, combined with the total thickness of the sensor layers, allows a marginal containment of the flux at the endcap-barrel interface. Large steel bridge bars cover the Layer 18 gap in azimuth. These bars are buried under the corner blocks. These massive corner blocks are separated from each other by a constant gap: they occlude fractionally less of the inner layers than the outer layers (see Fig. 21). The calorimeter is suspended from the horizontal corner blocks, and the magnet cryostat, with the magnet's radial and longitudinal restraining rods, from the diagonal corner blocks. The gaps between the corner blocks contain, in the case of the diagonal sextants, two gap filler plates which cover the RPC front end electronics, and a cable way which carries cables and services for the EMC, SVT and DCH and IFR. In the case of the top and bottom sextants, there is one center plate with gaps left for IFR cables and access to RPC front-end cards. RPC services run along the side plates of the sextant; they are also buried under the corner blocks. In the backward direction, access is further limited due to the attachment of the DIRC support system to the magnet. The center plates of the top and bottom sextants are locked behind this support system, as well at the top diagonal corner blocks.

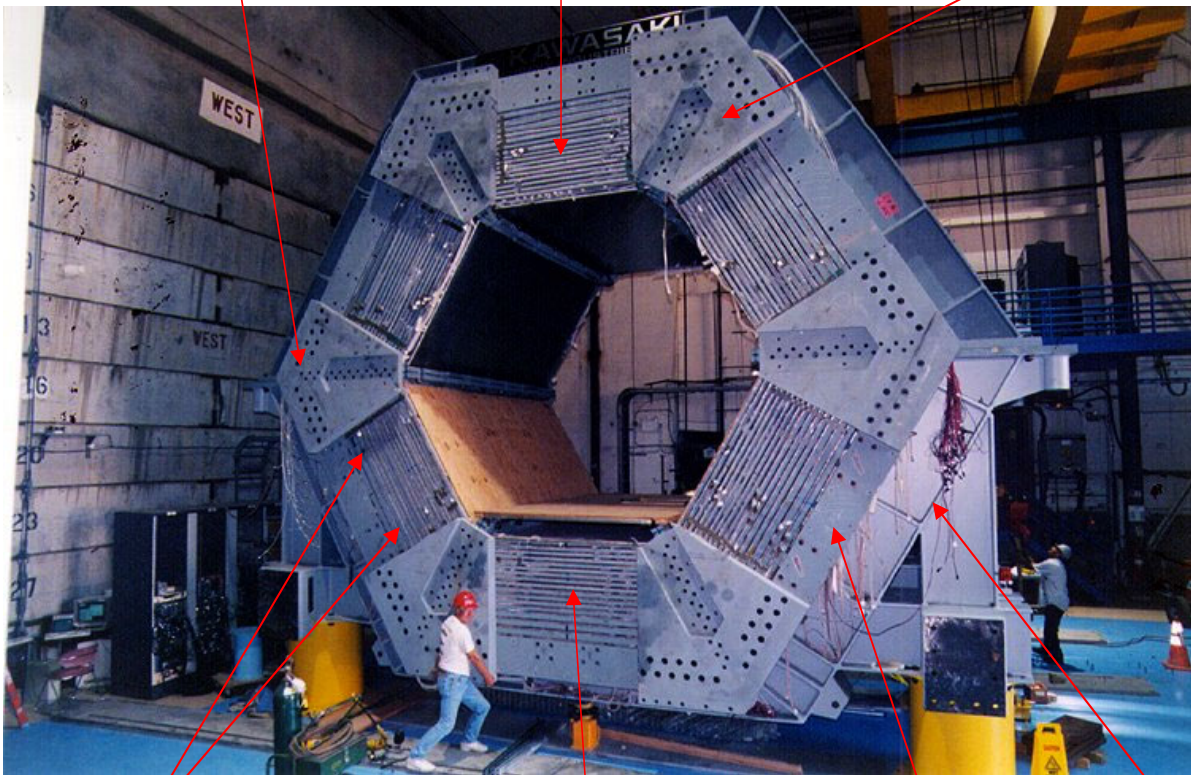
Because of the added constraints imposed by the DIRC support at the backward end, replacement of the RPCs will be performed at the forward end of the detector. In order to replace RPCs in diagonal sextants, the

Barrel Steel

horizontal corner block

gaps with trapped RPCs

diagonal corner block



location of gap filler plates

location of center plate

bridge bar

cradle

Figure 21: The barrel steel.

following sequence will take place. Gap filler plates are removed. This has been done frequently for repairs of IFR electronics, is straightforward and requires about one hour for each plate. Cables and services for the inner systems are disconnected at the detector end and pulled back across the IFR steel. For the SVT cable plant, which was designed to be easily disconnected so that the Forward Calorimeter endcap could be easily pulled back, the time to remove and re-establish cable connections is less than a week for the two sextants that these cables traverse. For the EMC, an estimate of three weeks total for four sextants has been made. This may prove to be an underestimate. DCH services consist of a few gas lines that are not a schedule driver. The magnet restraining rods are disconnected for the sextant. The corner block is then removed. Though procedures have not been detailed, this is not considered to be a high-risk operation. In order to remove the other corner block for the diagonal sextant, the calorimeter's load, which is carried by four supports, must be transferred off of one of these supports. This is a riskier operation than the comparable task for the magnet, though it is deemed to be possible without damage to the calorimeter. Substantial engineering is required before this can be done. After the load is transferred, the horizontal corner block is removed, followed by the Layer 18 bridge bar. Though the barrel preparations are complete, the forward end door must be moved beyond the end of its normal travel (off the drive screw) and the field-shaping plug must be removed so that the RPCs will clear the door. RPCs may then be removed, though service connections at the backward end of the RPCs are likely to slow this task. The new sensing element and absorber can be added and the process described above reversed in order to complete installation. In the case of the top and bottom sextants, the center plate is removed, the magnet restraints released and the corner blocks removed. There are few non-IFR services affected. After removal of the bridge bar, access is available to all RPC layers but Layer 19. Chamber removal is simple for the top sextant. For the bottom sextant, it is complicated by the presence of the column that supports the raft that contains beam line elements. This column, and the concrete and steel pedestal behind it, provide a longitudinal stop that requires RPC dismemberment on removal, and limits the width and length of the new sensor elements to be installed.

4.2 Engineering Issues

Issues that must be confronted include: enhanced earthquake movement due to installation of new absorber; rigidity of the magnet structure when the

corner blocks have been removed; load transfer for the magnet; and load transfer for the calorimeter.

Additional absorber must be added in IFR slots to compensate for the loss of absorber due to the inability to replace Layer 19. Calculations were performed, before this committee met, for 5 layers of 7/8" brass. The motion of the detector with respect to the floor slab and beam line elements, the strength of the floor slab and its susceptibility to punch-through, the performance of the earthquake isolators, the strength of the X and Z restraint rods and connections to the floor and barrel, and the connection of the Y restraint to the floor were all analyzed and found to be acceptable. The Earthquake Review committee provided a peer review assessment of this work; it concurred with the conclusions. However, five layers of brass is less than desired from a physics standpoint: increased absorber leads to decreased π contamination in the identified μ sample. Earthquake calculations were also performed for eight layers of additional brass absorber. In this case, the differential motion of the detector with respect to beam line elements was found to be unacceptable. Six additional layers of brass, configured like design BD2, appear to be acceptable. This conclusion awaits peer review.

A finite element analysis has been performed on a quarter model of the detector. In this analysis all the corner blocks were removed from the detector. Resulting deflections were found to be acceptable. A full detector analysis run assuming that no more than two of the twelve corner blocks are removed at any time yields acceptable deflections.

The engineers who designed the magnet and the calorimeter expect that the load transfer of part of the load for these systems is an acceptable operation. However, more detailed analysis is required.

Dead load deflections of the iron due to the weight of the added brass are currently under analysis. The deflections may impose additional constraints on the new sensing element thickness or require additional structures to ensure that the required gap is maintained.

Much of the complication and risk associated with the sensor replacement is due to the need to remove the corner blocks, which in turn is driven by the need to remove the large RPC chambers. If it were possible to destructively remove the RPCs, then the new sensors and absorber plates could be designed to be inserted into the IFR gaps without removing the corner plates. This scenario is attractive and was actively pursued, but no viable method was found to remove the RPCs without creating an unacceptable amount of debris in the detector.

5 Resistive Plate Chamber technology

The proposal by the RPC proponents would be to replace the active layers of the barrel IFR with double-gap RPCs (Fig. 22). The two gaps would be read out by a single pair of orthogonal cathodes in the same fashion as the original chambers, so that the detector signals would appear the same to the front-end electronics. The double-gap design reduces the sensitivity of the detector to random decreases of efficiency of any particular gap. Different high-voltage supplies would power each gap, further reducing the correlation. A prototype of the conceptual design has been successfully tested.

The chambers would be manufactured by General Technica in a manner similar to those installed in summer 2002. GT is fully booked producing chambers for LHC experiments, but it is plausible that *BABAR* would be able to obtain the required chambers by summer 2005.

This proposal would be the lowest cost of the three presented to the review committee. This is in part because of the nature of the technology, and also because it makes the best use of the existing infrastructure, including gas system, high voltage, front end electronics, and monitoring electronics.

There has been substantial work over the last several years on understanding the reasons for the degradation of the existing chambers and developing methods to counteract it. However, the physics and chemistry involved are still not well understood, and new issues—such as those observed during the examination of layer 7 of the November 2000 endcap chambers—continue to arise. For these reasons, and given the short time scale on which a decision is required, the review committee does not recommend RPCs for the barrel replacement.

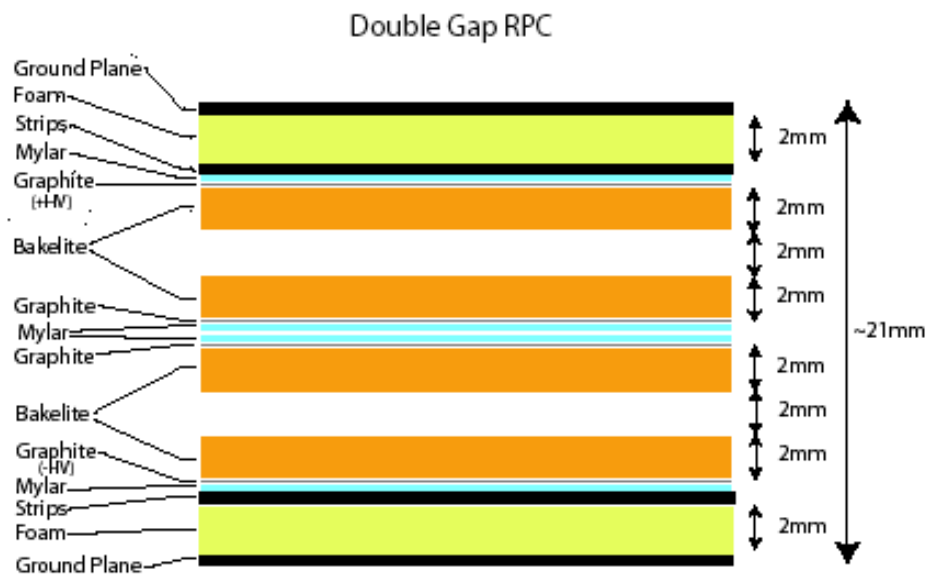


Figure 22: Conceptual design of the double-gap RPC proposed for the IFR barrel.

6 Limited Streamer Tube technology

6.1 LST Technology Overview

Limited Streamer Tubes (LSTs) were invented in the 1970's by Iarocci and coworkers. An LST consists of a resistive tube (the cathode) with a wire strung down the center (the anode). Positive high voltage is applied to the anode, with the cathode at ground. As the HV is increased the LST will go from proportional (avalanche) mode into limited streamer mode, characterized by the development of a streamer discharge on one side of the wire. This mode is also known as limited Geiger operation and it is characterized by large signals and a wide HV operating plateau. Resistive plastics are often used for the tubes so that an induced signal can be picked up on external conductive strips, avoiding the need to capacitively decouple the signal from the wire.

LSTs can be manufactured cheaply by fabricating a set of adjacent cells from a single piece of formed plastic, without a cover. The resistive coating is usually some form of graphite paint applied to the inside. The wires are laid down in the channels and supported by spacers, and then the cover is put in place. The resulting package of (typically) 8 cells is called a "tube" (Fig. 23). The efficiency of an LST tube is about 90% due to geometrical effects (wall thickness, spacers, dead regions in corners).

The main parameters in designing an LST system are the choice of cathode material and dimensions, the wire diameter, the gas mixture and the operating HV. There is an interplay among these parameters and certain choices have to be made. For example, the maximum rate is limited by the recovery time, which is dominated by after-pulsing caused when UV photons from the streamer cause emission of secondary electrons from the cathode (photo-electric effect). The delay for after-pulses depends on the tube geometry and the electron drift velocity in the gas. These after-pulses do not interfere with stable operation, they simply limit the maximum rate to typical rates of 100 Hz/cm², though this will depend on the tube dimensions and the gas composition.

It is desirable to operate LSTs with a wide HV plateau over which the singles rate remains relatively constant. As the fraction of the quenching component in the gas increases, this plateau widens and moves to higher voltage. However, the total amount of isobutane, which is often used as the quenching component, is limited by safety concerns.

Smaller diameter cells have a narrower stable region in the HV plateau due to increased after-pulsing. To remediate this, more quenching gas is

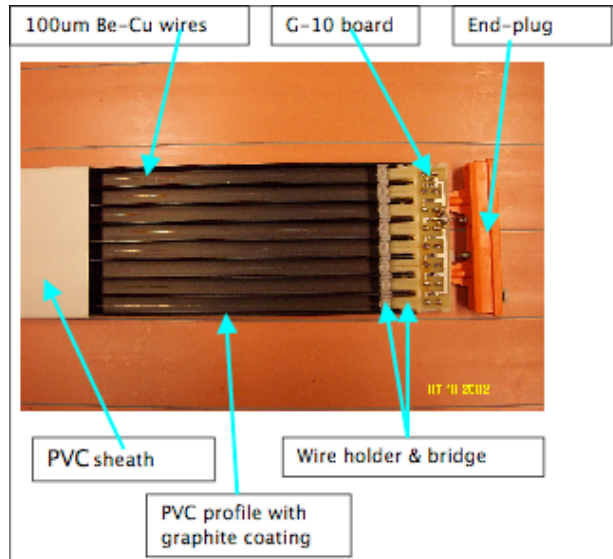


Figure 23: An LST tube with the top cover pulled back to reveal the major components

required, which then requires going to higher voltage. To reduce the HV, the wire diameter can be decreased, but thinner wires are less robust against breaking. Smaller cells are also more sensitive than larger cells to small displacements of the anode wire. For both of these reasons, bigger cells are more stable to operate.

For certain cathode materials, a self-sustaining discharge mode can occur. This is brought on when too much charge is produced within a given period of time. Basically, the positive ions drift back to the cathode and accumulate there. If too much charge piles up, the electric field in the insulator gets too high and breaks down, liberating electrons back into the gas mixture and initiating after-pulses in a self-sustaining fashion. This process is hard to stop once it gets going; the tube must be turned off and some time allowed for the charge to dissipate.

6.2 Robustness and Maturity

LSTs have been used in more than a dozen previous experiments. The most common geometry is 9 x 9 mm square cells. Total areas covered are several thousand square meters with tens of thousands of cells for the largest systems.

Most problems are due to flaws in initial tube construction. Infant mortality ranges from 4–30% depending on experiment, and annual failure rates from negligible to 2%/year. Most experiments use PVC coated with graphite paint. OPAL used BREOX B35 over the graphite paint, which improved performance. ZEUS used a material called Noryl ENV509 instead of PVC, and claimed improved aging performance.

LSTs have been tested up to 3C/cm with no loss of performance. This would take over 500 years in endcap layer 18 location.

6.3 LST proposal for *BABAR*

The baseline proposal is to use a double layer of 8 mm \times 9 mm PVC cells per gap, with a single set of orthogonal readout strips located outside the double layer. Prototype tests at Princeton indicate good efficiency for detecting minimum ionizing particles even if only a single layer produces a streamer discharge.

The prototype used in this test was produced by machining down standard 9 mm \times 9 mm tubes, a process that did not produce an entirely satisfactory device. For example, the anode wire was not centered in the resulting cells. The dies needed to produce the final tubes have been ordered but no prototypes have yet been tested. For this reason, the group continues to pursue an alternative solution that uses a single large-cell layer. The goal is to undertake the necessary tests to decide on the cell geometry by May 2003.

The tubes will be produced by Pol. Hi. Tech, with quality control procedures similar to those used to great success by Phenix.

To simplify testing, handling and replacement, 5–7 tubes will be assembled into a module, with several modules per layer. The 4.3 cm wide readout strips that run along the length of the tubes (“phi strips”) will be attached to each module. There will be a single set of 4 cm wide z strips for an entire layer, which will be produced as a single structure and inserted into the layer independently of the modules.

Position resolution is estimated to be better than 1 cm per layer in both directions. A simple TDC is proposed that would provide timing resolution of better than 100 ns on the OR of 16 channels. This would provide a significant background suppression relative to the 4 μ s trigger window currently used in the IFR.

New front end electronics will include signal amplification and variable thresholds. The interface to the existing IFR-FIFO boards will be the same as the existing electronics, so that these can be reused.

The high voltage system will be designed to minimize the impact of any chamber drawing high current. In particular, the two layers of tubes in a module will be supplied by different high voltage channels, and sufficient cables will be run from the distribution box to the detector to allow individual tubes to be disconnected if necessary. The proposed cable is high density and will fit in the existing cable trays. A single HV channel will power approximately four cables.

The gas will be the non-flammable Ar/C₄H₁₀/CO₂ (2.5/9.5/88) mixture used by SLD. The gas system will be simpler than the existing IFR system, with no buffer tank. It is expected that it will fit in the existing gas hut and connect to a spare gas line running from the gas hut to the detector. The gas will flow in parallel through the two layers in a module.

There is good progress on building a team that could deliver the system on time. Work has begun on a number of production details, including quality control and module assembly. The cost of the LST system is expected to be more than the RPC proposal but less than the scintillator.

7 Scintillator Technology

The proposed scintillator technology is based on an extruded scintillator strip detector design similar in many respects to that used in the MINOS experiment [1]. However, while MINOS uses photomultipliers to detect the scintillator light, this proposal would use avalanche photodiodes.

The design calls for extruded scintillator bars of ~ 5 cm width running the full length of the barrel in z . There would be 14 bars per module and three modules per layer. The resolution in $r\phi$ would therefore be better for inner layers, where multiple scattering of muons is less. Four 1.2 mm diameter wavelength-shifting fibers embedded in each bar would run to a light-mixer connected to a single $2\text{ mm} \times 2\text{ mm}$ pixel of a 4×4 avalanche photodiode array. One APD array would be located at each end of a module (Fig. 24), allowing both ends of the fibers to be read out. (The two unused pixels per array would be spares to allow for infant mortality in APD yield). Timing and pulse height information would be used to localize tracks in z with a resolution of approximately 20 cm.

Due to constraints of fiber bend radius and the limited cable tray space available, it is not possible to run the fibers to a region of low enough magnetic field to permit photomultipliers to be used.

Although avalanche photodiodes are in use elsewhere—for example, Hamamatsu photodiodes are used to read out the CMS WPbO_4 crystal calorimeter—the APD array is the most novel aspect of the proposal. The gain of the Hamamatsu device is 50–100, which is insufficient given the low light yield of the scintillator/WLS technology. The proposal is to instead use APD arrays supplied by RMD [5], which have a gain of 1000. The devices would be cooled to 0°C using Peltier coolers to improve noise performance. The modules would be flushed with a dry gas to stop condensation.

A full length (4 m) prototype of a single bar has been tested with a photomultiplier on one end and a single-pixel cooled APD on the other. The pulse height distribution for cosmic rays (Fig. 25) indicates good separation between signal and background even for tracks at the far end of the bar from the APD.

The readout of the APDs would require custom amplifiers, discriminators, and TDCs, together with an interface to the *BABAR* data acquisition system. The amplifiers will need to be carefully designed to preserve the timing information of the system and to have acceptable noise performance. It may be possible to reuse part of the design of the DIRC electronics.

The cost of the scintillator system would be the largest of the three proposals.



Figure 24: Mockup of one end of a scintillator/WLS fiber module. The nominal extent in z (the fiber direction) is 4 m. One APD array reads out the fibers at each end.

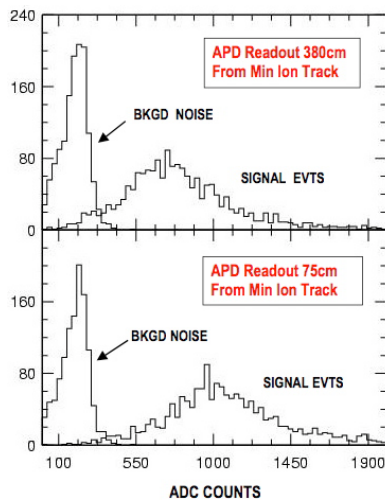


Figure 25: Pulse height spectrum for cosmic rays and for background noise for tracks passing through the scintillator 380 cm from the APD (top) or 75 cm from the APD (bottom).

The major concerns with respect to this technology are reliability and schedule. There has been no experience with the APD arrays and the associated issues of cross talk, efficiency, and the reliability of the light coupling. A particularly significant issue is the initial failure rate and lifetime (mean time between failures) of the APDs. A proposed accelerated aging test, performed with the APDs at elevated temperatures, would require of order 10 arrays at a cost of approximately \$30k.

The committee believes there is substantial schedule risk associated with verifying the suitability of the APD arrays and developing and building a complete detector system on the necessary time scale. For this reason, the committee does not recommend scintillator as the replacement technology for the IFR barrel.

References

- [1] MINOS Technical Design Report, NuMi Note NuMi-L-337, http://www-numi.fnal.gov/minwork/info/minos_tdr.html
- [2] Kuraray Corp., 3-10, Nihonbashi, 2 chome, Chuo-ku, Tokyo 103, Japan
- [3] ATLAS Tile Calorimeter Technical Design Report, CERN/LHCC 96-42, http://atlas.web.cern.ch/Atlas/SUB_DETECTORS/TILE/TDR/TDR.html
- [4] CMS Electromagnetic Calorimeter Technical Design Report, CERN/LHCC 97-33, <http://cmsdoc.cern.ch/cms/TDR/ECAL/ecal.html>
- [5] Model A1604, Radiation Monitoring Devices, Inc. Watertown, Massachusetts 02472.

8 Recommendations

1. In order to optimize the physics output for the next decade, *BABAR* should proceed with an upgrade to the Barrel IFR as soon as practical. This upgrade should include the following elements:
 - Removal of existing RPC Chambers.
 - Placement of 2.2 cm thick brass slabs into at least 5 slots (or 6 slots if possible, pending a final optimization of material placement and load restrictions).
 - Installation of detectors into the other 12–13 slots.
2. The detection system for the barrel upgrade should be double-gap LST chambers of 2.2 cm thickness. Pre-production double gap prototypes should be fabricated and thoroughly tested by May 1, 2003, and their performance reviewed immediately thereafter.
3. An ongoing internal review process is encouraged to provide timely review of technical, cost, schedule, and management issues associated with the upgrade.
4. The fabrication and installation of the Barrel upgrade should be optimized with respect to running schedules and other down time needs of PEP-II and *BABAR* so as to minimize the impact on the integrated luminosity.

A Organization of the IFR Barrel Replacement Committee

The working committee responsible for the review consisted of three components: a review committee, proponents for each technology, and consultants. The review committee consisted of C. Hearty and B. Ratcliff (co-chairs), F. Forti, Y. Karyotakis, J. Nash, J. Richman, N. Roe, B. Spaan, and J. Va'vra. There were two proponents for each of the three technologies considered: R. Calabrese and C. Lu for limited streamer tubes, H. Band and F. Ferroni for resistive plate chambers, and D. Hitlin and R. Schindler for scintillator.

The consultants were J. Krebs (engineering), F. O'Neill (safety), and G. Cavoto, D. Lange, and A. Mohapatra (physics simulation).

The committee was formed during the *BABAR* collaboration meeting in London in September 2002. Much of the information was presented during workshops held Nov. 14–15, 2002 and Dec. 8 and 11, 2002. The working and review committees also held several phone meetings. Each technology submitted written proposals and answered detailed questions.

Two aspects of the review were not specific to a particular technology. Jim Krebs oversaw the engineering effort on the removal of the existing RPC chambers and the additional of brass. Jeff Richman organized the analysis of the physics cost of the degradation of the existing chambers and the benefits of replacing them.

B Charge to the IFR Barrel Replacement Review Committee

October 10, 2002

The performance of the Instrumented Flux Return has been declining since turn-on. Recognized sources of efficiency loss include problems with heating of the resistive plate chambers (RPCs) during *BABAR*'s Run 1 and with Q/C during construction. The endcap RPCs are now in the process of being replaced with new RPCs, and substantial additions in brass and steel have been made to improve the muon identification and pion rejection, with small compromise in K_L^0 identification.

It is now time to deal with the IFR barrel. Attempts at remediation of RPC barrel performance have stretched the expected lifetime of the current modules. However, it is expected that continued efficiency decline in these chambers will lead to inability to identify muons and K_L^0 in the barrel in less than three years. The hope is to begin upgrade of the barrel IFR in summer 2004 during the normal two-month shutdown, with completion of the barrel in the long shutdown in summer 2005. Recent understanding of RPC limitations suggest that another endcap IFR intervention may also be needed as early as 2005–6.

The IFR Upgrade Committee has been assembled to consider the IFR upgrades through the balance of this decade, the natural life of this experiment. The Working Committee consists of the Review Committee, which is charged with developing a recommendation to *BABAR* Management and the Technical Board concerning the upgrade; the group of those advocating particular solutions for the sensor technology for the upgrade; and consultants who will help in evaluation and understanding the consequences of upgrade scenarios. The first group is composed of: C. Hearty and B. Ratcliff (co-chairs); F. Forti, Y. Karyotakis, J. Nash, J. Richman, N. Roe, B. Spaan and J. Va'vra, members. The second group includes H. Band, R. Calabrese, F. Ferroni, D. Hitlin, C.-G. Lu and R. Schindler. The consultants are G. Cavoto, H.J. Krebs and D. Lange. Other consultants may be added if need arises.

The review committee should aim to report its recommendations in early January, in time for the International Finance Committee meeting. The committee should take this goal into consideration in developing the time line for its efforts. In the event that the committee is unable to identify a clear choice of technology at the time of the IFC meeting, they are asked to propose a plan that allows the decision to be made as soon as practical

thereafter, and provide an envelope for the cost.

The committee should advise on improvements that can be made to the muon identification in the barrel IFR based on the foreseeable physics goals of the experiment. In particular, this includes improvements in pion rejection due to increased material inserted in the barrel gaps in place of sensing layers. The committee should revisit the issue of muon identification/pion rejection efficiency versus K_L^0 identification/veto efficiency and provide a clear statement of priorities for the IFR.

The committee should consider backgrounds due to PEP-II operations, assuming that the machine component upgrade occurs in 2005-2006 and that these lead to a maximum luminosity of $4 \times 10^{34} \text{ cm}^{-2}\text{s}^{-1}$ during the final years of the experiment.

The barrel gaps each contain a monolithic RPC that consists of three gas gaps laid out longitudinally. This design was developed to minimize costs and acceptance losses due to dead material. The consequence is that the RPCs are trapped behind the corner blocks needed to support the *BABAR* hexagonal structure. Preliminary finite element analyses indicate that it is possible to remove these corner pieces, though feasibility of calorimeter load transfer has not yet been verified. Techniques have been considered for destructive removal of chambers from the gaps without corner block removal. The committee is asked to comment on progress in these efforts, and on their viability based on the associated risks.

There are now three technologies proposed for the barrel upgrade. These include RPCs, limited streamer tubes (LSTs)(Iarocci tubes), and scintillator strips read out with avalanche photodiodes. The committee should characterize the effectiveness and robustness of the system that would result from each of these technologies. This picture should include evaluations of resolution, number of layers needed for reliable muon/pion separation and identification, response to backgrounds, detector aging and radiation damage, and modularity for simplicity of repairs. The committee should evaluate the maturity of these technologies. The Review Committee is asked, in light of these considerations, to recommend to *BABAR* Management and the Technical Board its choice of technology for the IFR upgrade.

The IFR has a substantial electronics plant. The committee should consider the advisability of making use of this plant. The committee should comment on the ability of the technology options to use this plant, and to use designs and components from other systems or experiments. Estimates of electronic engineering required should be reported.

The IFR upgrade is the major construction project for *BABAR* for the next few years. This is a time of tight budgets. The proponents should

develop, and the committee comment on, cost estimates for each of the options. The committee should identify the hurdles in the sensor development paths. Schedules for production of sensor elements and needed manpower should be evaluated. The committee is asked to provide feedback on the feasibility of the proposed two-phase (2004 and 2005) upgrade plan. Comments on availability of institutional support would be welcome. The committee is asked to advise *BABAR* Management on the management of the upgrade enterprise, in particular with respect to recommendations concerning reviews during the construction phase.